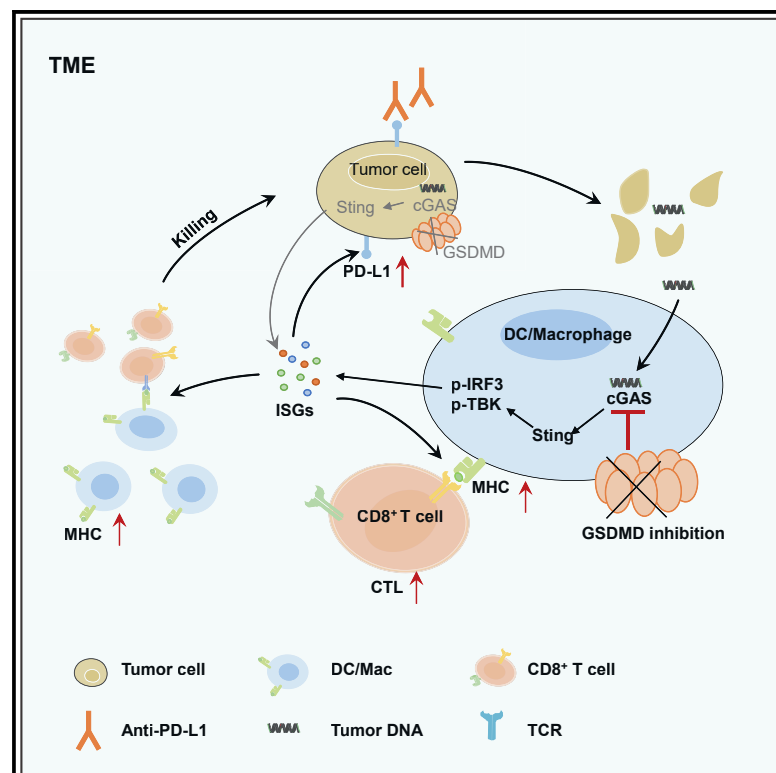


Gasdermin D restricts anti-tumor immunity during PD-L1 checkpoint blockade

Graphical abstract



Authors

Yuying Jiang, Yongbing Yang, Yingchao Hu, ..., Xi Wang, Zhibin Hu, Shuo Yang

Correspondence

bingweiwang@njucm.edu.cn (B.W.),
xiwang@njmu.edu.cn (X.W.),
zhibin_hu@njmu.edu.cn (Z.H.),
shuoyang@njmu.edu.cn (S.Y.)

In brief

Jiang et al. show that GSDMD positively correlates with immune checkpoint signature. Loss of GSDMD in APCs promotes CD8⁺ T cell activity through the upregulation of ISG program and thus enhances anti-tumor immunity during PD-L1 inhibition, highlighting the potential strategy of combining GSDMD/PD-L1 inhibition for immunotherapy.

Highlights

- GSDMD positively correlates with the immune checkpoint signature in tumor
- GSDMD is highly expressed in antigen-presenting cells (APCs) in tumor
- GSDMD deficiency in APCs promotes CD8⁺ T cell anti-tumor response through ISG program
- GSDMD inhibitors improve anti-tumor immunity during anti-PD-L1 treatment



Article

Gasdermin D restricts anti-tumor immunity during PD-L1 checkpoint blockade

Yuying Jiang,^{1,7} Yongbing Yang,^{1,7} Yingchao Hu,^{1,7} Rui Yang,¹ Jiajia Huang,⁴ Yi Liu,¹ Yuqing Wu,^{1,6} Sheng Li,¹ Chunmei Ma,¹ Fiachra Humphries,⁵ Bingwei Wang,^{4,*} Xi Wang,^{2,*} Zhibin Hu,^{2,3,*} and Shuo Yang^{1,8,*}

¹Department of Immunology, State Key Laboratory of Reproductive Medicine, Jiangsu Key Lab of Cancer Biomarkers, Prevention and Treatment, Collaborative Innovation Center for Personalized Cancer Medicine, Gusu School, Nanjing Medical University, Nanjing 211166, China

²State Key Laboratory of Reproductive Medicine, Nanjing Medical University, Nanjing 211166, China

³Department of Epidemiology, Center for Global Health, School of Public Health, Nanjing Medical University, Nanjing 211166, China

⁴Department of Pharmacology, Nanjing University of Chinese Medicine, 138 Xianlin Avenue, Nanjing 210023, China

⁵Department of Medicine, UMass Chan Medical School, Worcester, MA 01605, USA

⁶Department of Laboratory Medicine, The First Affiliated Hospital of Nanjing Medical University, National Key Clinical Department of Laboratory Medicine, Nanjing 210029, China

⁷These authors contributed equally

⁸Lead contact

*Correspondence: bingweiwang@njucm.edu.cn (B.W.), xiwang@njmu.edu.cn (X.W.), zhibin_hu@njmu.edu.cn (Z.H.), shuoyang@njmu.edu.cn (S.Y.)

<https://doi.org/10.1016/j.celrep.2022.111553>

SUMMARY

Tumor microenvironments (TMEs) require co-operation of innate and adaptive immune cells, which influence tumor progression and immunotherapy. Caspase-activated gasdermins facilitate tumor death and promote anti-tumor immunity. How pyroptosis in immune cells affects the TME remains unclear. TME expression of gasdermin D (GSDMD) is highly expressed in antigen-presenting cells (APCs) and correlates with immune checkpoint signatures. Through conditional deletion of GSDMD, we demonstrate that GSDMD in TME APCs restricts anti-tumor immunity during PD-L1 inhibition. Loss of GSDMD in APCs enhances interferon-stimulated genes (ISGs), thereby promoting CD8⁺ T cell activation in a cGAS-dependent manner. Moreover, pharmacological inhibition of GSDMD-mediated pyroptosis and PD-L1 improve anti-tumor immunity, highlighting the potential of combining GSDMD/PD-L1 inhibition for immunotherapy as a therapeutic strategy.

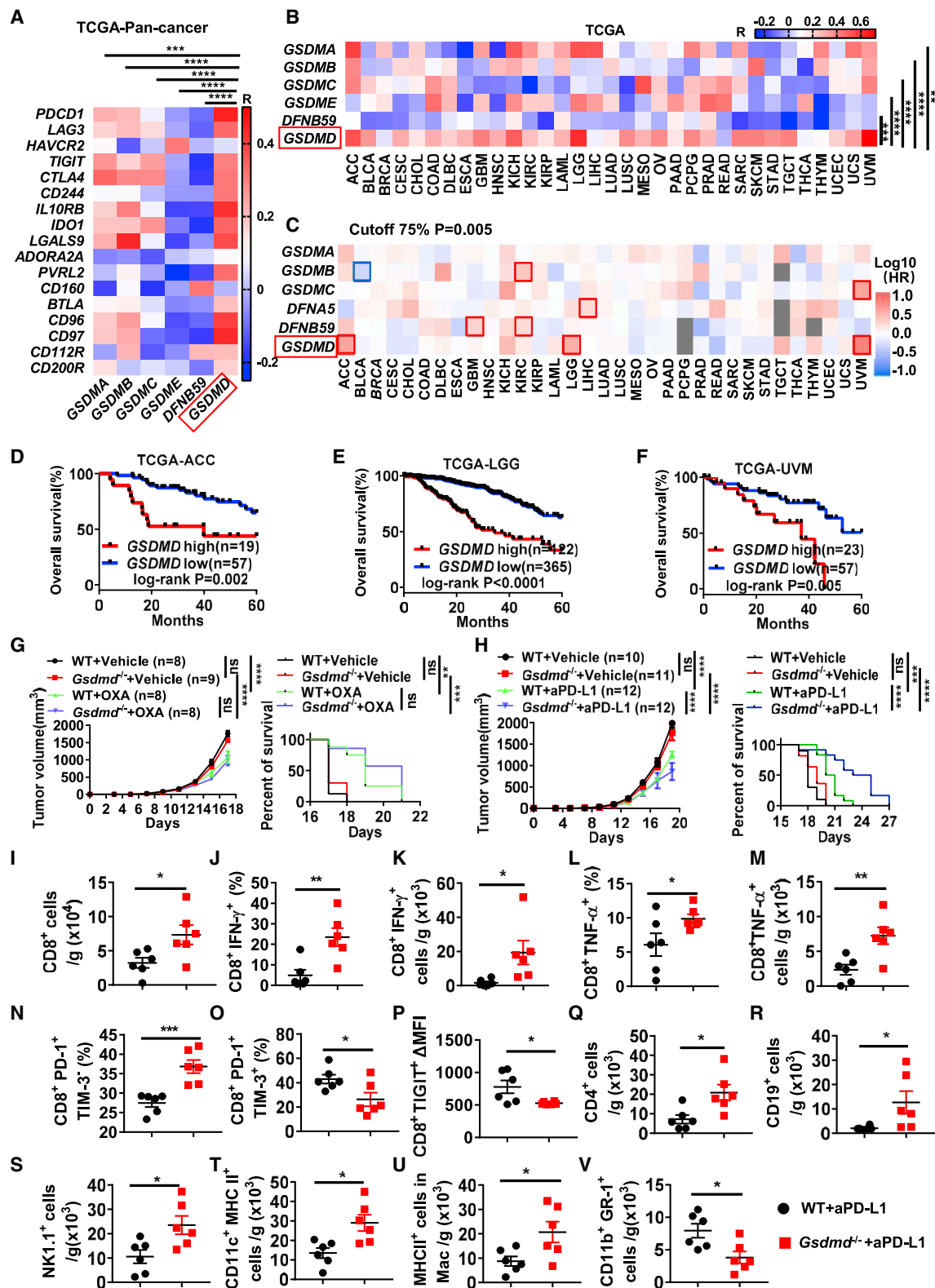
INTRODUCTION

The complex, dynamic composition of the tumor immune microenvironment (TME) requires the joint co-operation of innate and adaptive immune cells, which influence the initiation of the tumor, its progression, and the responsiveness to immunotherapies (Feng et al., 2019; Zhang and Zhang, 2020). Among these, the maintenance of activated cytotoxic CD8⁺ T cells (CTLs) in the TME is critical for the suppression and clearance of tumor cells (Farhood et al., 2019; Miller et al., 2019). However, continuous exposure to tumor antigen and dysregulation of inflammatory signals results in the terminal differentiation of CD8⁺ T cells and the induction of a dysfunctional state called “exhaustion” (Wherry and Kurachi, 2015). Exhausted CD8⁺ T cells characteristically express inhibitory receptors such as programmed cell death 1 (PD-1) or T cell immunoglobulin and mucin-containing molecule 3 (TIM-3) and display a distinct T cell state associated with tumor progression and impaired clearance of tumor cells (Thommen et al., 2018). Thus, elucidation of the key restriction pathways and underlying mechanism that limit CD8⁺ T cell anti-tumor immunity is essential for improving anti-tumor responsiveness.

Innate immune myeloid cells such as tumor-associated macrophages (TAMs), dendritic cells (DCs) and myeloid-derived suppressor cells (MDSCs) are important components of the TME. Myeloid cells participate in tumor antigen presentation, form the inflammatory TME and provide immune checkpoint inhibitory ligands, which regulate CD8⁺ T cell effector function and exhaustion (Fu and Jiang, 2018; Maimela et al., 2019). Additionally, TAMs and MDSCs promote tumor progression through production of tumor cell survival signals, angiogenesis, and by promoting invasion and metastasis (Grivennikov et al., 2010).

Inflammasomes are innate cytosolic multimeric complexes that assemble following detection of danger-associated molecular patterns (DAMPs) by intracellular sensor proteins such as NLRP3 and AIM2. Inflammasome assembly triggers the downstream activation of inflammatory caspases which cleave pro-IL-1 β and pro-IL-18 precursors into their mature forms (Bergsbaken et al., 2009; Rathinam et al., 2012). Caspase activation also triggers the induction of an inflammatory form of cell death termed pyroptosis via the proteolytic activation of GSDMD. Cleavage of GSDMD liberates its N-terminal fragment, which oligomerizes and forms membrane pores, leading to loss of plasma membrane integrity (Feng et al., 2019; Liu et al., 2016).





(legend on next page)

Inflammasomes are activated by a diverse range of DAMPs such as extracellular ATP, double-stranded DNA, and reactive oxygen species (ROS) and play crucial in the initiation of inflammatory responses in myeloid cells (Schroder and Tschopp, 2010). Increasing evidence suggest that inflammasome and pyroptotic responses play important and contrasting roles in regulating the TME and tumorigenesis (Dixon et al., 2021; Han et al., 2021; Van Deventer et al., 2010). Indeed, IL-1 β promotes the recruitment of MDSCs to tumors and facilitates tumor growth, metastasis, and angiogenesis (Tu et al., 2008). However, inflammasomes have also been reported to limit carcinogenesis by triggering pyroptosis in pre-malignant cells (Zitvogel et al., 2012). Specially, with the aid of perforin (PFN), granzyme A/B (GzmA/B) from cytotoxic lymphocytes are delivered into the cytoplasm of tumor cells to activate GSDMB/E directly or by inducing caspase-3 activation, leading to tumor cell pyroptosis (Zhang et al., 2020; Zhou et al., 2020). Pyroptotic tumor cells subsequently direct the TME toward anti-tumor immune responses through release of DAMPs and cytokines (Inoue and Tani, 2014).

Although the roles of gasdermin protein-mediated tumoral pyroptosis in anti-tumor immunity have been revealed, how pyroptosis in immune cells regulates anti-tumor activity and CD8⁺ T cell function in the TME remains unclear. Here, we found that GSDMD plays an important role in suppressing CD8⁺ T cell anti-tumor immunity, and GSDMD-induced pyroptosis in TME APCs inhibits ISG expression and impairs antigen presentation in response to anti-PD-L1 treatment.

RESULTS

GSDMD is highly expressed in myeloid cells and positively correlates with the immune checkpoint signature

Recent studies have reported on the roles of gasdermin-mediated pyroptosis in tumor cells (Zhang et al., 2020; Zhou et al., 2020). To further explore the role of gasdermin proteins in immune cells in the TME, we first analyzed the expression of gas-

dermin proteins (including GSDMA, GSDMB, GSDMC, GSDMD, DFNA5 [also known as GSDME], and DFNB59) in various immune cells from publicly available gene databases. Analysis of ImmGen (<https://www.immgen.org/>) and BioGPS (<http://biogps.org/>) databases revealed high levels of GSDMD expression in myeloid cells in both mouse and human compared with other gasdermins (Figures S1A–S1D). We next investigated the correlation of gene expression profiles between gasdermin family members and immune checkpoints (ICs) in pan-cancer RNA sequencing (RNA-seq) data of The Cancer Genome Atlas (TCGA). The expression of GSDMD was positively correlated with IC genes, including *PDCD1*, *LAG3*, *HAVCR2*, *TIGIT*, *CTLA4*, *CD244* (*PDL1*), *IL10RB*, *IDO1*, *LGALS9*, *ADORA2A*, *PVRL2*, *CD160*, *BTLA*, *CD96*, *CD97*, *CD112R*, and *CD200R* in pan-cancer data (Figure 1A). We termed the above immune checkpoint genes as a signature and further showed that the expression of GSDMD was most positively correlated with the immune checkpoint signature compared with other gasdermin family members both in pan-cancer and in 33 other cancer datasets (Figures 1B and S1E). We then mined public cancer gene expression and prognosis databases using the Gene Expression Profiling Interactive Analysis 2 (GEPIA2) web server (<http://gepia2.cancer-pku.cn/>) that analyzes the data from the TCGA database (Tang et al., 2019). Among 33 different cancer types, a negative correlation associated with GSDMD expression, and its corresponding prognosis value was shown in adrenocortical carcinoma (ACC), low-grade glioma (LGG), and uveal melanoma (UVM) at a cutoff of 75% or 50% high expression threshold (Figures 1C–1F, S1F, and S1G). Thus, these data demonstrate that GSDMD might regulate myeloid cell to affect anti-tumor immunity.

GSDMD deficiency enhances anti-tumor immunity under treatment with PD-L1 antibody

Given that B16F10 melanoma cells express very low levels of GSDMD protein (Figure S1H), we used a B16F10 melanoma engraftment model in wild-type (WT) and *Gsdmd*^{−/−} mice to

Figure 1. GSDMD expression correlates positively with an immune checkpoint signature, and its deficiency enhances responsiveness to PD-L1 inhibition

(A) Correlation analysis of gene expression profiles between gasdermin family members and immune checkpoints (ICs) in tumors from pan-cancer clinical data of the TCGA database. Pearson *r* values are shown in heatmap.

(B) Immune checkpoint genes in (A) were termed as IC signature, and correlation of gene expression profiles among gasdermin family members and IC signatures from 33 types of tumors in the TCGA database were analyzed. Pearson *r* values are shown in heatmap.

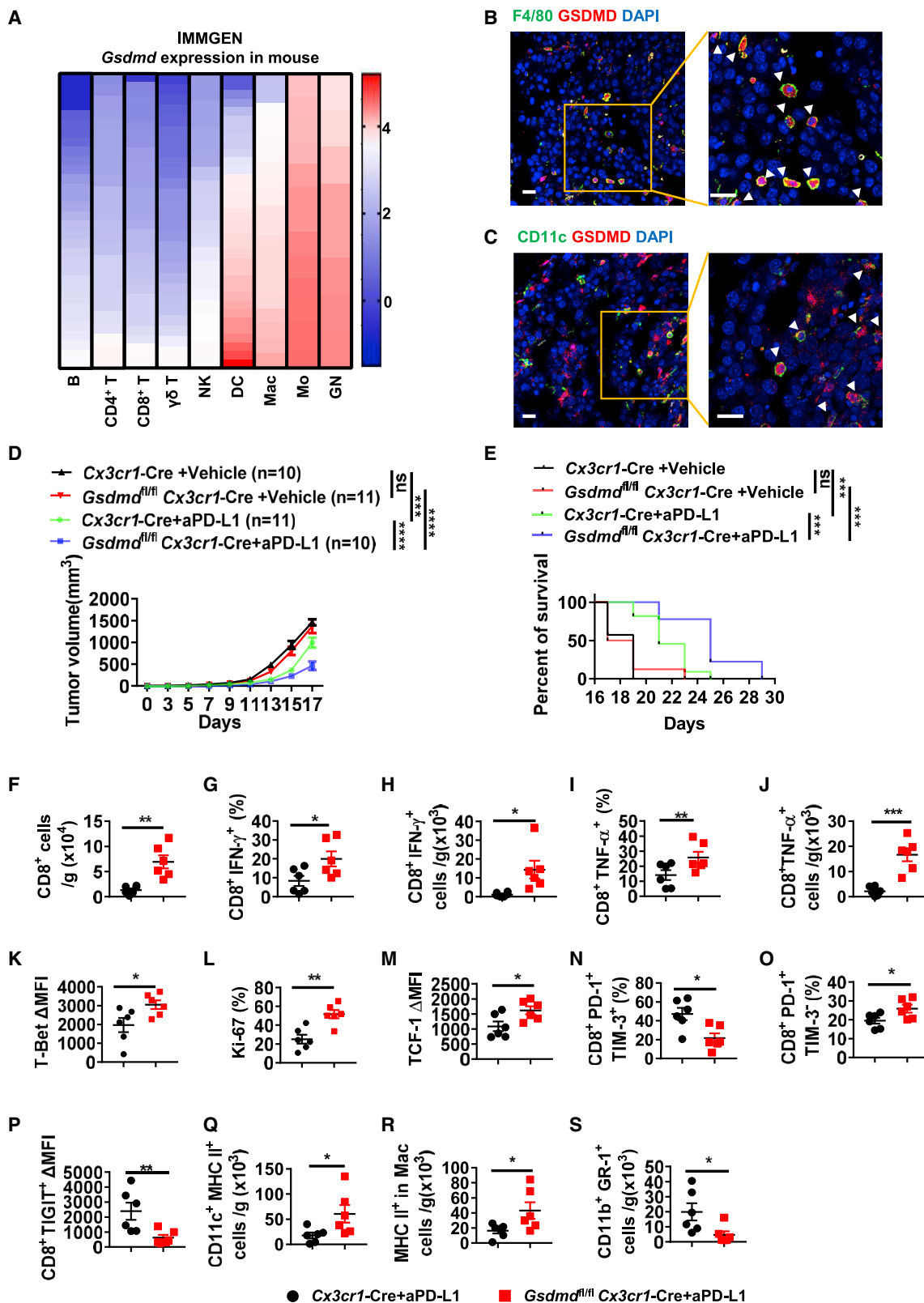
(C) Survival map of six human gasdermins from 33 types of tumors using GEPIA2. Gasdermin expression in all tumors from TCGA data was scored, and top 25% and low 75% were considered as high and low expression (at a cutoff of 75%), respectively. The blue square indicates that low expression of indicated gene was correlated with poor survival of patients (*p* < 0.005), and the red square indicates that high expression of indicated gene was correlated with poor survival of patients (*p* < 0.005).

(D–F) Kaplan-Meier plot of overall survival of patients with adrenocortical carcinoma (ACC), low-grade glioma (LGG), and uveal melanoma (UVM) on the basis of *Gsdmd* expression levels from TCGA data at cutoff 75%.

(G and H) WT and *Gsdmd*^{−/−} mice were implanted subcutaneously (s.c.) with B16F10 cells, OXA (G), aPD-L1 (H), or vehicle was administrated, and growth of B16F10 melanomas and survival of mice were assessed.

(I–V) WT and *Gsdmd*^{−/−} mice (*n* = 6 mice per group) were implanted subcutaneously (s.c.) with B16F10 cells and were treated with aPD-L1 on days 4 and 8. After 14 days, tumors were collected for analysis of tumor-infiltrating immune cells by flow cytometry: (I) numbers of CD8⁺ T cells; (J–M) percentages and numbers of IFN- γ ⁺ and TNF- α ⁺ cells in CD8⁺ T cells; (N and O) percentages of PD-1⁺ TIM-3[−] and PD-1⁺ TIM-3⁺ populations in CD8⁺ T cells; (P) mean fluorescence intensity (MFI) of TIGIT in CD8⁺ T cells; (Q–S) numbers of CD4⁺ T cells, CD19⁺ cells, and NK1.1⁺ cells in tumor microenvironment; and (T–V) numbers of DCs, MHC II⁺ macrophages, and MDSCs cells.

Data are pooled from three independent experiments for (G)–(V). Error bars show mean \pm SEM. **p* \leq 0.05, ***p* \leq 0.01, ****p* \leq 0.001, and *****p* \leq 0.0001; ns, not significant. Two-tailed paired Student's *t* test for (A) and (B). Log rank test for (D)–(F) and mice survival in (G) and (H). Two-way ANOVA for tumor size in (G) and (H). Two-tailed unpaired Student's *t* test for (I)–(V). See also Figures S1 and S2.



(legend on next page)

investigate how GSDMD regulates the host myeloid cell immunomodulation of tumor cells. However, GSDMD deficiency did not affect tumor progression (Figures 1G and 1H). We next treated tumor-bearing mice with the anticancer drug oxaliplatin (OXA) and anti-PD-L1 (Figures S2A and S2B). OXA treatment improved anti-tumor effects in both wild-type and *Gsdmd*^{-/-} mice, but there is no significant difference in tumor volume or survival observed between WT and *Gsdmd*^{-/-} mice (Figure 1G). Interestingly, *Gsdmd*^{-/-} mice treated with anti-PD-L1 significantly suppressed tumor progression and elevated mice survival compared with WT (Figures 1H and S2C), suggesting GSDMD negatively regulates the anti-tumor effect of anti-PD-L1 treatment. Moreover, immunofluorescence and fluorescence-activated cell sorting (FACS) analysis demonstrated that PD-L1 expression was significantly elevated in *Gsdmd*^{-/-} mice and mainly co-expressed with melanocytes (Figure S2D–S2G), which may explain why GSDMD deficiency only promotes anti-tumor immunity in response to anti-PD-L1 treatment.

To further explore the effect of GSDMD on anti-tumor immunity, we quantified the immune cell population in the TME (Figure S2H). In line with our previous data, GSDMD deficiency resulted in a significant increase in CD8⁺ T cell number in tumors from *Gsdmd*^{-/-} mice undergoing anti-PD-L1 treatment (Figures 1I and S2I). In addition, GSDMD deficiency resulted in the upregulation of IFN- γ , TNF- α , and PD-1⁺ TIM-3⁻ cells and downregulation of TIM-3 and TIGIT expression in CD8⁺ T cells (Figures 1J–1P and S2J–S2M). Total numbers of CD4⁺ T cells, B cells, and natural killer (NK) cells were also elevated in *Gsdmd*^{-/-} mice (Figures 1Q–1S, S2N, and S2O). Moreover, GSDMD deficiency led to the reduction of Treg cells in tumors (Figure S2P). Additionally, we observed a significant increase in the abundance of MHC II⁺ DCs and MHC II⁺ macrophages, which presented antigen and facilitated the recruitment of CD8⁺ effector and functional T cells to suppress tumor progression (Movahedi et al., 2010; Norian et al., 2009) (Figures 1T, 1U, S2Q, and S2R). A decrease in the number of myeloid-derived suppressor cells was observed in *Gsdmd*^{-/-} mice (Figures 1V and S2S). Furthermore, higher protein levels of IFN- γ (Figure S2T) and TNF- α (Figure S2U), but lower protein levels of IL-1 β (Figure S2V) and IL-18 (Figure S2W), were detected in tumors from *Gsdmd*^{-/-} mice with anti-PD-L1 synergistic treatment compared with WT mice. Collectively, these data indicate that

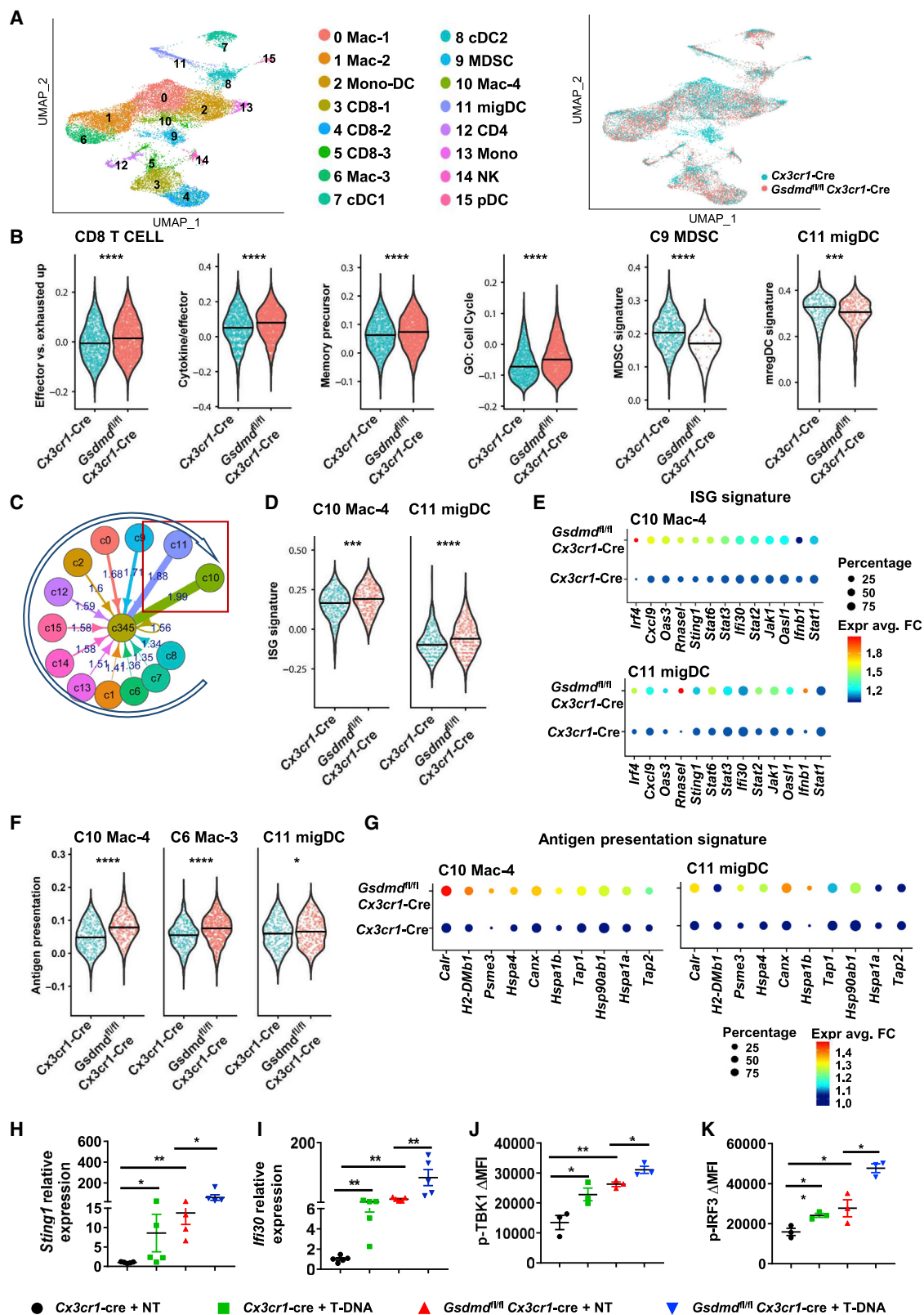
GSDMD negatively regulates anti-tumor immunity and impairs responsiveness to anti-PD-L1 treatment.

GSDMD deficiency in antigen-presenting cells, such as macrophages and DCs, promotes anti-tumor response

Expression analysis of ImmGen (<https://www.immgen.org/>) and European Molecular Biology Laboratory (EMBL) databases (<https://www.ebi.ac.uk/>) revealed that macrophages and DCs were the primary source of GSDMD (Figures 2A, S1A, and S3A). Using confocal microscopy to assess the B16F10 TME, we further showed that GSDMD staining co-localized with F4/80⁺ macrophage and CD11c⁺ DCs (Figures 2B and 2C) but not with T cells (Figure S3B), indicating that GSDMD suppresses the effects of anti-PD-L1 treatment via antigen-presenting cells of myeloid cells. To test this, we crossed *Gsdmd*^{fl/fl} mice with *Cx3cr1*-Cre mice to delete GSDMD in APCs, including macrophages and DCs. In line with constitutive deletion of GSDMD, conditional deletion of GSDMD APCs did not alter tumor progression (Figures 2D, 2E, and S3C). However, when treated with anti-PD-L1, GSDMD deficiency in APCs significantly reduced tumor progression (Figures 2D and 2E). In line with these results, we determined tumor-infiltrating immune cells in day 14 (Figure S3D) and observed a significant expansion of CD8⁺ T cells, especially IFN- γ ⁺ and TNF- α ⁺ CD8⁺ T cells, in tumors from *Gsdmd*^{fl/fl} *Cx3cr1*-Cre mice compared with *Cx3cr1*-Cre controls (Figures 2F–2J and S3E–S3G). Furthermore, increased T-bet, Ki-67, and TCF-1 expression was observed in tumor derived CD8⁺ T cells from *Gsdmd*^{fl/fl} *Cx3cr1*-Cre mice (Figures 2K–2M and S3H–S3J), indicating an enhanced cytotoxic T cell response and stem-like feature (Dixon et al., 2021). Consistently, GSDMD deficiency in APCs increased PD-1⁺ TIM-3⁻ non-exhausted population and decreased PD-1⁺ TIM-3⁺ exhausted populations among tumor CD8⁺ T cells. Decreased expression of the inhibitor receptor TIGIT was also found in *Gsdmd*^{fl/fl} *Cx3cr1*-Cre mice (Figures 2N–2P, S3K, and S3L). Moreover, elevated numbers of DCs and MHC II⁺ macrophages, and lower numbers of MDSCs, were observed in *Gsdmd*^{fl/fl} *Cx3cr1*-Cre mice compared with control mice (Figures 2Q–2S and S3M–S3O). Enhanced protein levels of IFN- γ and TNF- α were also observed in tumors from *Gsdmd*^{fl/fl} *Cx3cr1*-Cre mice (Figures S3P and S3Q). Thus, all these data suggest that GSDMD in antigen-presenting cells negatively regulates the expansion of antigen-presenting cells and cytotoxic CD8⁺ T cells in response to anti-PD-L1 treatment.

Figure 2. GSDMD deficiency in antigen-presenting cells promotes anti-tumor responses

(A) Expression of gasdermin family genes in immune cells from publicly available gene databases ImmGen (<https://www.immgen.org/>).
(B) Immunofluorescence staining for GSDMD (red) and F4/80 (green) in tumor tissue from WT mice. Scale bars, 20 μ m. The white arrowheads indicate GSDMD⁺ and F4/80⁺ co-expression cells.
(C) Immunofluorescence staining for GSDMD (red) and CD11c (green) in tumor tissue from WT mice. Scale bars, 20 μ m. The white arrowheads indicate GSDMD⁺ and CD11c⁺ co-expression cells.
(D and E) *Cx3cr1*-Cre and *Gsdmd*^{fl/fl} *Cx3cr1*-Cre mice were implanted subcutaneously (s.c.) with B16F10 cells and were treated with aPD-L1 or vehicle at indicated time points, and the growth of B16F10 melanomas (D) and survival of mice (E) were assessed.
(F–S) *Cx3cr1*-Cre and *Gsdmd*^{fl/fl} *Cx3cr1*-Cre mice (n = 6 mice per group) were implanted subcutaneously with B16F10 cells, treated with aPD-L1 on days 4 and 8. Tumors were collected on day 14 and analyzed using flow cytometry for the total numbers (F), percentages and numbers of IFN- γ ⁺ (G and H) and TNF- α ⁺ cells (I and J) in CD8⁺ T cells, expression of T-bet (K), Ki-67 (L), Tcf-1 (M), percentages of PD-1⁺ TIM-3⁻ (N) and PD-1⁺ TIM-3⁺ (O) populations, and expression of TIGIT (P) in CD8⁺ T cells. (Q–S) Numbers of DCs, MHC II⁺ macrophages, and MDSCs cells from tumors on day 14.
Data are representative of three independent experiments for (A) and (B). Data are pooled from three independent experiments for (D)–(S). Error bars show mean \pm SEM. *p \leq 0.05, **p \leq 0.01, ***p \leq 0.001, and ****p \leq 0.0001; ns, not significant. Two-way ANOVA for tumor size and log rank test for survival in (D) and (E). Two-tailed unpaired Student's t test for (F)–(S). See also Figure S3.



(legend on next page)

GSDMD deficiency boosts CD8⁺ T cell anti-tumor immunity by upregulating ISG program of APCs

In order to explore the underlying mechanism by which GSDMD suppresses anti-tumor immunotherapy in APCs, we performed single-cell RNA-seq (scRNA-seq) on immune cells extracted from the TME. An unbiased clustering approach was used to partition cell types into 16 clusters, which were visualized using uniform manifold approximation and projection (UMAP) and labeled by known markers for the cell subtypes (Figures 3A and S4A). Single-cell RNA-seq survey showed that the tumor immune cells between control and *Gsdmd*^{fl/fl} *Cx3cr1*-Cre mice were clearly demarcated (Figure 3A). Consistent with our previous FACS data, CD8⁺ T cells (clusters 3–5) from tumors in GSDMD-deficient mice expressed higher levels of gene signatures found in a spectrum of functional states, including effector, cytokine, memory precursor and cell cycle (Best et al., 2013; Dixon et al., 2021) (Figure 3B). In addition, GSDMD-deficient mice displayed lower rate and gene signatures of inhibitory MDSCs (cluster 9) and migratory DCs (migDCs) (cluster 11) compared with control mice (Figures 3A, 3B, and S4A). Notably, these cells play an inhibitory role to anti-tumor CD8 T cells in the TME (Dixon et al., 2021; Gabrilovich, 2017; Maier et al., 2020). As CD8⁺ T cells are the key component in anti-tumor processes, we next explored which cell types in the TME can regulate CD8⁺ T cell function. Cell-cell communication inference was performed on scRNA-seq data using the CellChat algorithm (Jin et al., 2021), which scored the communication between different cell types and CD8⁺ T cells. Our analysis revealed that the Mac-4 (cluster 10) and migDC (cluster 11) exhibited the most significant level of crosstalk with CD8⁺ T cells (Figure 3C). Interestingly the Mac-4 and migDC clusters were also characterized by an ISG signature (Figure S4A). Moreover, Mac-4 and migDC cells in tumors from GSDMD-deficient mice expressed higher levels of ISGs compared with control (Figures 3D and 3E). Notably, scRNA-seq data revealed that crosstalk between Mac-4 or migDCs with CD8⁺ T cells occurred via antigen presentation related ligand-receptor pairs (Figure S5A). Consistent with this, previous studies have demonstrated that IFN-stimulated response can promote antigen presentation (Gobin et al., 1999). Indeed, our scRNA-seq data also showed that macrophages and DCs in

tumors from GSDMD-deficient mice expressed an antigen-presenting signature (Figures 3F and S5B) and related genes at a much higher level (Figures 3G and S5C). We further sorted myeloid cells (excluding MDSCs) from tumors and stimulated them with cell-free tumor DNA (transfer DNA) from B16F10 cells and performed qPCR (Figures 3H–3I, S5D, and S5E) and flow cytometry analysis (Figures 3J, 3K, S5F, and S5G). Higher levels of ISGs and phosphorylated TBK1 and IRF3 were observed in antigen-presenting cells from the tumor of GSDMD-deficient mice compared with controls. Thus, these data indicate that GSDMD regulates ISG expression in APCs to suppress antigen presentation and CD8⁺ T cell anti-tumor immunity.

GSDMD activation in TME partially depends on AIM2 inflammasome

In a previous report, AIM2 inflammasome inhibition was an effective strategy to improve the efficacy of melanoma immunotherapy by promoting STING-induced type I IFN secretion (Fukuda et al., 2021). We further compared pyroptotic cell death in APCs from *Aim2*^{fl/fl} *Cx3cr1*-Cre, *Gsdmd*^{fl/fl} *Cx3cr1*-Cre and *Cx3cr1*-Cre mice in the B16F10 melanoma model to explore the role of AIM2 inflammasome in GSDMD activation in the TME. We observed a reduction of caspase-1/11⁺ propidium iodide (PI)⁺ tumor APCs from *Aim2*^{fl/fl} *Cx3cr1*-Cre mice when compared with *Cx3cr1*-Cre mice but a higher number of pyroptotic APCs in *Aim2*^{fl/fl} *Cx3cr1*-Cre mice relative to *Gsdmd*^{fl/fl} *Cx3cr1*-Cre mice (Figures S6A and S6B). These data indicate that the AIM2 inflammasome is activated and partially required for GSDMD-mediated pyroptosis of tumor APCs in the TME. Because of the limited number of APCs in tumors, we further assessed the role of the AIM2 inflammasome in pyroptotic cell death and GSDMD activation in bone marrow-derived macrophages (BMDMs) following transfer DNA stimulation. Notably, we found that GSDMD cleavage and pyroptosis were not completely blocked in *Aim2*^{fl/fl} *Cx3cr1*-Cre cells (Figures S6C and S6D), further suggesting that tumor DNA (T-DNA)-induced GSDMD activation is only partially dependent on AIM2 inflammasome activation. Altogether, our data suggest that the AIM2 inflammasome is only partially required for GSDMD activation and there may be other upstream signaling that regulate the activation of GSDMD in the TME.

Figure 3. GSDMD deficiency boosts CD8⁺ T cell anti-tumor immunity by enhancing ISG expression in APCs

(A) Unsupervised clustering of scRNA-seq data of immune cells in tumor microenvironment (n = 20,410 single-cell transcriptomes, from two independent experiments; cells were pooled from 3 mice for each experiment). Unsupervised clusters are overlaid on the UMAP map and are labeled according to the expression signature of cell type-specific marker genes (left). Cells from *Cx3cr1*-Cre (blue dots) or *Gsdmd*^{fl/fl} *Cx3cr1*-Cre (red dots) mice are also plotted as indicated (right). (B) Single-sample gene set enrichment analysis (ssGSEA) for indicated signature of indicated cell types. (C) Cell-cell communication inference on the basis of the scRNA-seq data using the CellChat algorithm. Numbers indicated the scores of communications between different cell types by assessing the averaged expression of ligands, receptors, and their cofactors in each cell type. (D) ssGSEA analysis for ISG signature of indicated cell types. (E) Bubble plot showing the gene expression related to ISG signature of indicated cell types from *Cx3cr1*-Cre and *Gsdmd*^{fl/fl} *Cx3cr1*-Cre mice. (F) ssGSEA analysis for antigen presentation signature of indicated cell types. (G) Bubble plot showing the gene expression related to antigen presentation signature of indicated cell type from *Cx3cr1*-Cre and *Gsdmd*^{fl/fl} *Cx3cr1*-Cre mice. (H–K) *Cx3cr1*-Cre and *Gsdmd*^{fl/fl} *Cx3cr1*-Cre mice were implanted subcutaneously with B16F10 cells and intraperitoneally injected with aPD-L1 on days 4 and 8. Fourteen days later, Lin[−] CD11b⁺ Gr1[−] myeloid cells were sorting from tumors and stimulated for 12 h *in vitro* by cell-free tumor DNA (T-DNA) from B16F10 cells. Cells were then collected for qPCR analysis of *Sting1* (H), *IFI30* (I), and flow cytometry analysis of p-TBK1 (J) and p-IRF3 (K). Data are pooled from three independent experiments for (H)–(K). Error bars show mean ± SEM. *p ≤ 0.05, **p ≤ 0.01, ***p ≤ 0.001, and ****p ≤ 0.0001. Two-tailed unpaired Student's t test for (B), (D), (F), and (H)–(K). See also Figures S4–S7.

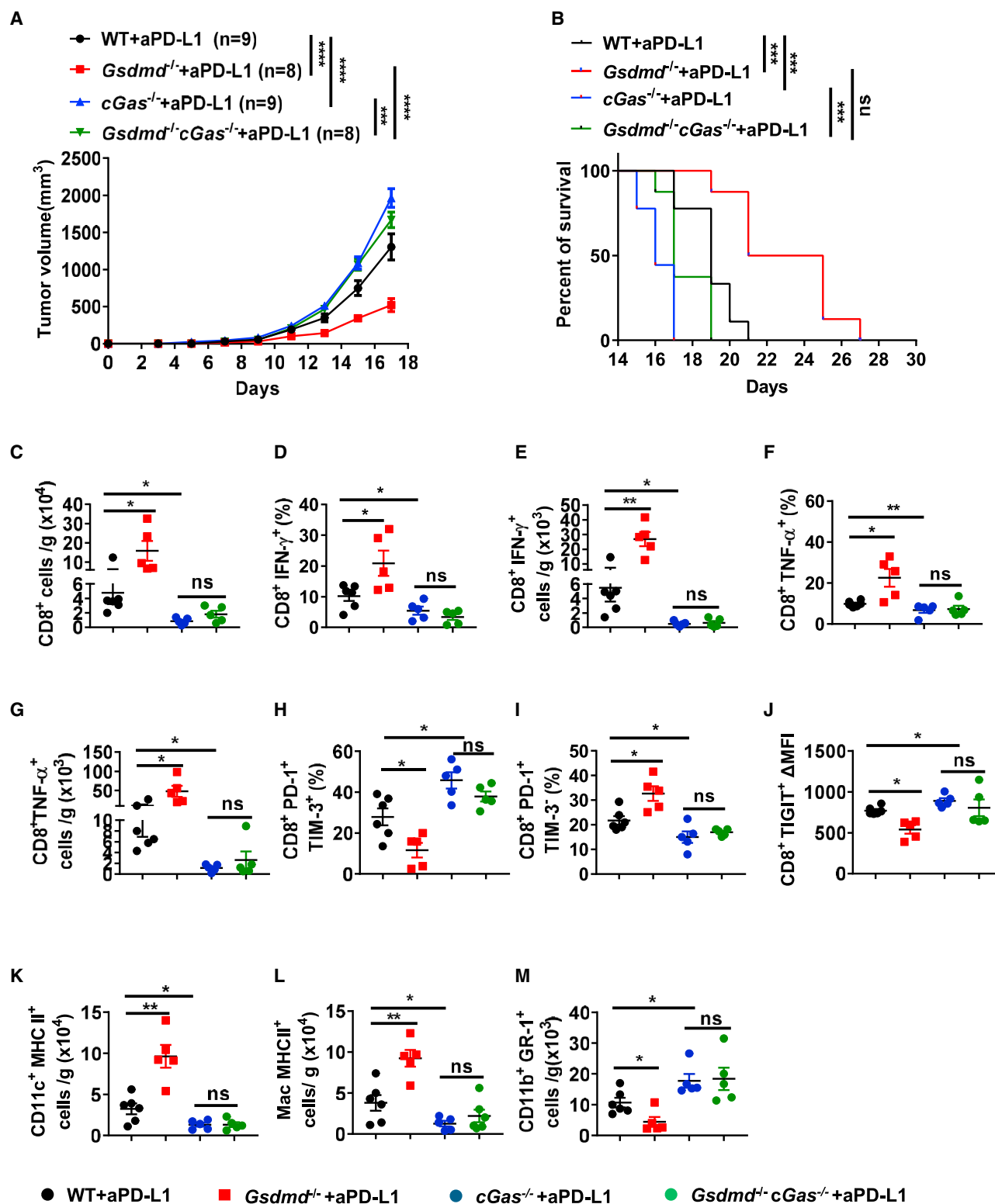


Figure 4. GSDMD deficiency enhances cGAS-dependent anti-tumor immunity in response to anti-PD-L1 treatment

(A and B) WT (n = 9), *Gsdmd*^{-/-} (n = 8), *cGas*^{-/-} (n = 9), and *Gsdmd*^{-/-} *cGas*^{-/-} (n = 8) mice were implanted subcutaneously with B16F10 cells and intraperitoneally injected with aPD-L1 on days 4 and 8. The growth of B16F10 melanomas in mice (A) and the survival of mice (B) were assessed.

(legend continued on next page)

Transfer-DNA-induced GSDMD-mediated inhibition of cGAS-STING signaling is dependent on both pyroptosis and K⁺ efflux

We also cultured primary macrophages and treated the cells with transfer DNA, and found that the cleavage of GSDMD, release of LDH, p-TBK1, and expression of ISG were significantly upregulated in response to transfer DNA (Figure S7). Moreover, GSDMD deficiency significantly increased the expression of ISG and p-TBK1 following transfer DNA stimulation (Figures S7C–S7F and S7I–S7L). These data are consistent with a negative role for GSDMD in the cGAS-STING signaling pathway. To investigate the negative effect of pyroptosis by GSDMD on cGAS-STING signaling, we treated the cells with dimethyl fumarate (DMF), which suppresses the cleavage and activation of GSDMD (Humphries et al., 2020). As expected, transfer-DNA-induced GSDMD cleavage and LDH release was significantly inhibited by DMF treatment (Figures S7A and S7B). In addition, DMF treatment enhanced T-DNA-induced ISG expression and p-TBK1 in WT cells to a level comparable with *Gsdmd*^{−/−} cells with or without DMF treatment (Figures S7C–S7F), thus suggesting that GSDMD negatively regulates T-DNA-induced cGAS-STING signaling via pyroptosis. To further explore the role of K⁺ efflux in the negative regulation of cGAS signaling by GSDMD (Banerjee et al., 2018), we assessed the role of K⁺ efflux using KCl to block K⁺ efflux in transfer DNA stimulated cells. We found that GSDMD cleavage and LDH release by transfer DNA were not affected following KCl treatment (Figures S7G and S7H). In addition, we found that ISG expression and p-TBK1 was upregulated both in WT and *Gsdmd*^{−/−} cells under treatment with KCl. However, the supplement of KCl only decreased but did not block the enhanced ISG expression and cGAS-STING signaling in *Gsdmd*^{−/−} cells compared with WT (Figures S7I–S7L). Thus, these data indicate that GSDMD deficiency promotes T-DNA-induced cGAS-STING signaling through a mechanism which is partially dependent on K⁺ efflux inhibition. Collectively, our data suggest that GSDMD-induced pyroptosis attenuates the activation of cGAS-STING signaling following transfer DNA stimulation in a K⁺ efflux-dependent and -independent manner *in vitro*.

GSDMD deficiency enhances cGAS-dependent anti-tumor immunity in response to anti-PD-L1 treatment

Previous studies have identified GSDMD as a negative regulator of cGAS-mediated inflammation in colitis and *F. novicida* bacterial infection (Banerjee et al., 2018; Ma et al., 2020). Antigen-presenting cells in the TME have been reported to endocytose extracellular tumor DNA resulting in the activation of the cGAS-STING signaling pathway and induction of the ISG response (de Mingo Pulido et al., 2021). Thus, we next generated *Gsdmd*^{−/−}*cGas*^{−/−} (double knockout [DKO]) mice to determine if the tumorigenic function of GSDMD occurs through suppression of cGAS-dependent anti-tumor immunity. Tumor burden in DKO mice was comparable with *cGas*^{−/−} mice in response

to anti-PD-L1 treatment. Reductions in tumor size and increased survival rates observed in GSDMD-deficient mice were lost in DKO mice (Figures 4A and 4B). Consistent with this, cell number and the levels of IFN- γ and TNF- α among tumor CD8⁺ T cells were significantly reduced in DKO mice compared with *Gsdmd*^{−/−} mice (Figures 4C–4G and S8A–S8C). The expression of exhaustion-associated markers, such as TIM-3 and TIGIT, was also elevated (Figures 4H–4J and S8D, and S8E). In addition, the abundance of DCs and MHC II⁺ macrophages were reduced in DKO mice (Figures 4K, 4L, S8F, and S8G), accompanied by a pronounced expansion of MDSCs (Figures 4M and S8H). Overall, these data demonstrate that GSDMD promotes tumor progression through inhibition of the cGAS pathway.

GSDMD in tumor cells also restrains anti-tumor immunity

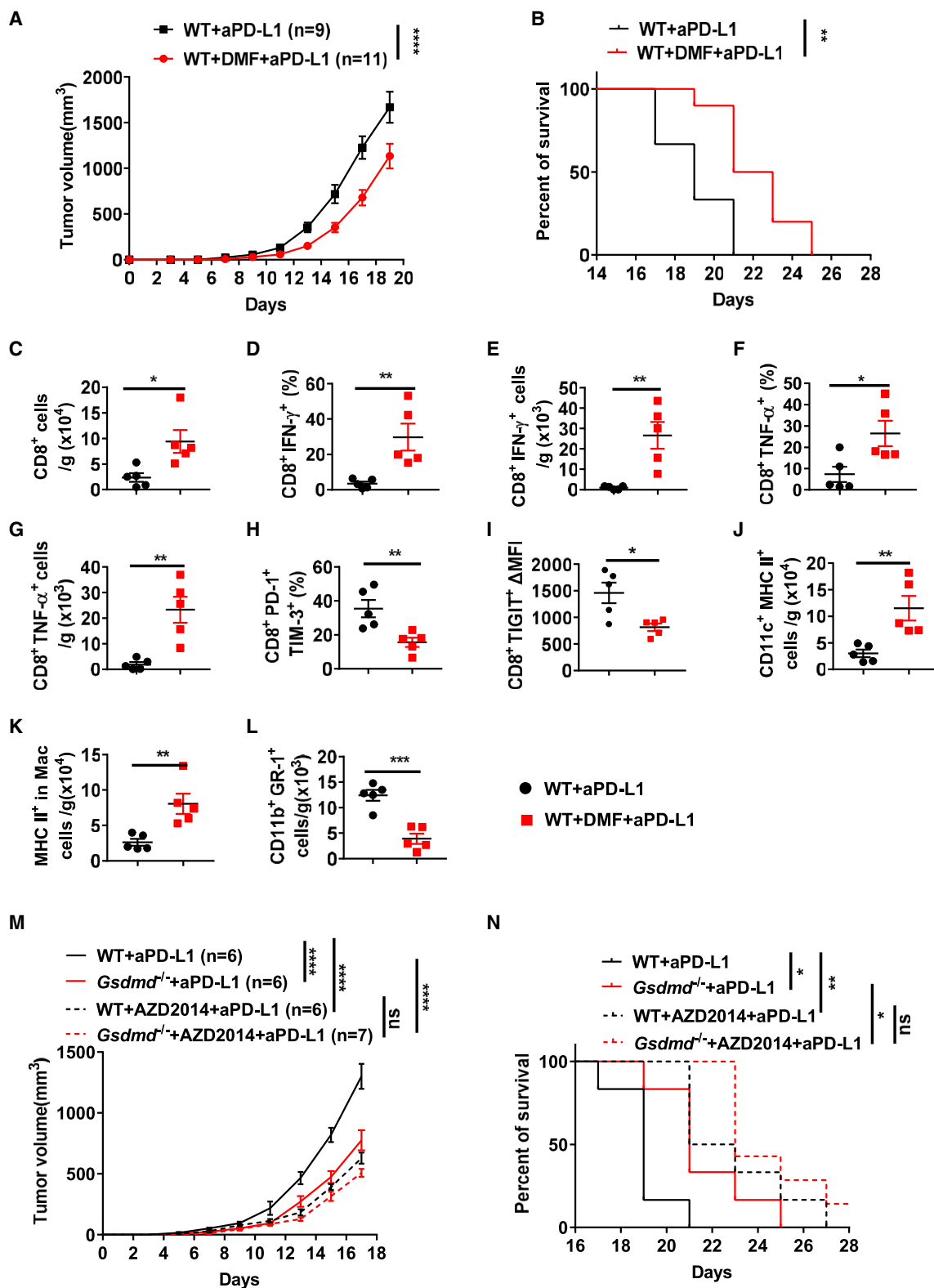
Gasdermin proteins are also expressed in tumor cells. We processed whole-transcriptome data from the Cancer Cell Line Encyclopedia (CCLE) data portal (<https://sites.broadinstitute.org/ccle/>) to analyze the expression of gasdermin family members in tumor cells. Our data analysis revealed that GSDMD is highly expressed in 33 different tumor cells compared with other gasdermin family members (Figures S9A–S9F), indicating that GSDMD may also exert effect in tumor cells. Thus, we overexpressed and knocked down GSDMD in B16F10 melanoma cells and MCA205 fibrosarcoma cells, respectively, to investigate the function of GSDMD in tumor cells (Figures S10A and S10C). The change of GSDMD expression did not alter the proliferative capacity of tumor cells (Figures S10B and S10D). When engrafted into WT mice, B16F10 melanoma cells overexpressing GSDMD impaired the response to anti-PD-L1 treatment compared with mice engrafted with native B16F10 melanoma cells (Figures S10E and S10F). In addition, flow analysis showed a decrease in the number of cytotoxic CD8⁺ T cells (Figures S10G–S10J and S11A–S11C), MHC II⁺ DCs (Figures S10L and S11E), and MHC II⁺ macrophages (Figures S10M and S11F) and an increase in exhausted CD8⁺ T cells (Figures S10K and S11D) as well as MDSCs (Figures S10N and S11G) in B16F10 tumor cells expressing GSDMD. Moreover, the expression of ISGs were lower in tumors from mice engrafted with GSDMD-overexpressed cells compared with control (Figure S11H). In contrast, mice engrafted with GSDMD-knockdown MCA205 tumor cells expressing GSDMD-specific short hairpin RNA (shRNA), tumor development was greatly reduced and immune cell profiles and the ISG expression signature in the tumor were elevated (Figures S10O–S10X and S11I–S11P). Thus, these data indicate that GSDMD also suppresses intrinsic anti-tumor activity.

Pharmacological inhibition of GSDMD-mediated pyroptosis significantly improves anti-tumor immunity in combination with PD-L1 antibody treatment

Previous studies have reported that dimethyl fumarate suppresses the cleavage and activation of GSDMD (Humphries

(C–M) Fourteen days after B16F10 cells implantation, tumors were collected for flow cytometry analysis of CD8⁺ T cells (C–J), DCs (K), MHC II⁺ macrophages (L), and MDSCs (M).

Data are pooled from three independent experiments for (A)–(M). Error bars show mean \pm SEM. * $p \leq 0.05$, ** $p \leq 0.01$, *** $p \leq 0.001$, **** $p \leq 0.0001$; ns, not significant. Two-way ANOVA test for tumor size and log rank test for survival in (A) and (B). Two-tailed unpaired Student's *t* test for (C)–(M). See also Figures S8–S11.



(legend on next page)

et al., 2020). To further confirm the effect of GSDMD-mediated pyroptosis in tumor progression, we inhibited GSDMD activation in melanoma-bearing mice by administering DMF (Figure S12A). Administration of DMF reduced tumor burden and increased survival in response to anti-PD-L1 treatment (Figures 5A and 5B). Consistently, the abundance of total CD8⁺ T cells and cytokine-producing CD8⁺ T cells were increased (Figures 5C–5G and S12B–S12D), but exhausted characteristics were downregulated (Figures 5H, 5I, S12E, and S12F) after DMF therapy. Moreover, DMF and anti-PD-L1 synergistic treatment elevated the abundance of antigen-presenting cells including DCs and MHC II⁺ macrophages and decreased the number of MDSCs in the tumor (Figures 5J–5L and S12G–S12I). In addition, the mTORC1 pathway has recently been reported to mediate GSDMD-induced pyroptosis (Evavold et al., 2021). Thus, we also administrated the mTORC1/2 inhibitor AZD2014 to suppress pyroptosis in WT and GSDMD-deficient mice. WT mice treated with AZD2014 had reduced tumor sizes and survival comparable with GSDMD-deficient mice (Figures 5M, 5N, and S12J). Collectively, these data further indicate that inhibition of GSDMD-mediated pyroptosis improves anti-tumor immunity during anti-PD-L1 treatment.

DISCUSSION

PD-L1 checkpoint blockade is a frontline treatment for numerous cancers with a large number of clinical trials ongoing. Despite this remarkable therapy, a large number of patients fail to respond to anti-PD-L1 therapy. With combination therapies are now becoming more common to overcome host-restriction factors. Indeed, elucidation of the key restriction pathways that limit anti-tumor immunity in response to checkpoint blockade is essential for improving responsiveness and expanding PD-L1 inhibition to tumor types. In this study, our data show that GSDMD functions as a restriction factor to PD-L1 checkpoint blockade and can suppress the ability of macrophages and DCs to present tumor-associated antigens and the following anti-tumor effects of CD8⁺ T cells by targeting the cGAS pathway and inhibiting ISG expression mainly in APCs in the TME (Figure S13C).

Previous studies have shown GSDMB/E-mediated tumor cell pyroptosis can promote anti-tumor immunity during cytotoxic lymphocyte-induced killing (Zhang et al., 2020; Zhou et al., 2020), thus highlighting the important anti-tumor functions of gasdermin proteins. In contrast, we show that GSDMD is highly expressed in macrophages and dendritic cells and promotes tumor progression through inhibiting anti-tumor immunity. In addition, GSDMD restriction of anti-tumor immunity only occurred

during checkpoint blockade with GSDMD-deficient mice displaying comparable tumor growth with untreated WT mice. Previous studies have demonstrated that GSDMD restricts cGAS activation and ISG via potassium efflux following AIM2 activation (Banerjee et al., 2018). Notably, ISG expression can induce the expression of PD-L1 on tumors, which in turn attenuates the cytotoxic T cell response (Yang et al., 2014). Indeed, enhanced ISG expression is coupled to enhanced expression of PD-L1 on tumors in GSDMD-deficient mice (Figures S2C–S2F), which might attenuate the cytotoxic T cell response and counteract any enhancement of anti-tumor immunity by ISG upregulation. Thus, GSDMD loss only significantly affects anti-tumor immunity in response to anti-PD-L1 therapy. In support of this, loss of cGAS or STING fails to effect tumor progression (Wang et al., 2017). Altogether, these findings highlight the functional diversity, complexity, and interdependence of gasdermin family proteins in regulating anti-tumor immunity.

Moreover, optimistic outcomes of patients with ACC, LGG, and UVM were observed to be inversely correlated with GSDMD expression. Unfortunately, there was no information on immune checkpoint therapies with respect to ACC, LGG, and UVM from TCGA. However, the expression of *CD274* and *PDCD1* was relatively lower in ACC, LGG, and UVM on the basis of the TCGA database (Figures S13A and S13B). Additionally, there are reports showing that PD-1/PD-L1 blockade is not an effective treatment for patients with gliomas (Wang et al., 2019), uveal melanoma (Algazi et al., 2016) and adrenocortical carcinoma (Le Tourneau et al., 2018). Thus, patients with ACC, LGG, and UVM may not be significantly affected by PD-1 signaling and thus are insensitive to PD-1/PD-L1 blockade. In contrast, the low expression of GSDMD is markedly responsible for the survival of patients.

Using scRNA-seq and *Gsdmd*^{−/−} *cGas*^{−/−} mice, we uncovered that GSDMD negatively regulates anti-tumor immunity during checkpoint blockade by suppressing cGAS-dependent ISG expression in APCs. These data are consistent previous reports demonstrating the negative regulatory role of GSDMD playing in cGAS-mediated inflammation during colitis and *F. novicida* infection (Banerjee et al., 2018; Ma et al., 2020). Interestingly, phagocytosis of tumor derived DNA triggers cGAS activity in APCs and initiates strong anti-tumor effects when subjected to stresses including checkpoint blockade (Feng et al., 2019; Wang et al., 2017). Moreover, cGAS-mediated ISG expression promotes the maturation of APCs and enhances cross-presentation of tumor-associated antigens to CD8⁺ T cells (Xia et al., 2016). Consistently, we found that the antigen-presenting expression signature was greatly enhanced in *Gsdmd*^{−/−} TME APCs.

Figure 5. Pharmacological inhibition of GSDMD enhances checkpoint blockade responsiveness

(A and B) WT mice were implanted subcutaneously with B16F10 cells and intraperitoneally injected with aPD-L1 (n = 7) or aPD-L1 and DMF (n = 11). The growth of B16F10 melanomas (A) and the survival of mice (B) were assessed.

(C–L) Fourteen days after B16F10 cells implantation, tumors were collected for flow cytometry analysis of CD8⁺ T cells (C–I), DCs (J), MHC II⁺ macrophages (K), and MDSCs (L).

(M and N) WT and *Gsdmd*^{−/−} mice were implanted subcutaneously with B16F10 cells and intraperitoneally injected with aPD-L1 (n = 6 mice per group) or aPD-L1 and AZD2014 (n = 6 WT and 7 *Gsdmd*^{−/−} mice). The growth of B16F10 melanomas (M) and the survival of mice (N) were assessed.

Data are pooled from three independent experiments for (A)–(N). Error bars show mean ± SEM. *p ≤ 0.05, **p ≤ 0.01, ***p ≤ 0.001, and ****p ≤ 0.0001; ns, not significant. Two-way ANOVA for tumor size and log rank test for survival in (A), (B), (M), and (N). Two-tailed unpaired Student's t test for (C)–(L). See also Figures S12 and S13.

Reactive oxygen species are enriched in the TME, including in myeloid cells, which contributes to tumor progression (Kashyap et al., 2019). Interestingly, ROS modulation has been implicated in inflammasome activation and pore formation downstream of GSDMD cleavage (Evavold et al., 2021). Thus, ROS accumulation in the TME may directly influence the pore-forming activity of GSDMD and tumor progression. Moreover, we investigate the possible role of AIM2 inflammasome in GSDMD-mediated pyroptosis in tumor APCs but found AIM2 inflammasome is partially required for GSDMD activation, thus further suggesting there may be other upstream signaling mechanisms that regulate the activation of GSDMD in the TME. Treatment of DMF which suppresses the activation of GSDMD significantly improved T-DNA-induced ISG expression *in vitro* and anti-tumor immunity *in vivo*, suggesting that GSDMD negatively regulated cGAS-STING signaling primarily through its pyroptotic effect. In addition, GSDMD pore formation has been previously attributed to negatively regulating cGAS activity and ISG responses by reducing intracellular K⁺ efflux (Banerjee et al., 2018). Here we found that GSDMD deficiency promoted T-DNA-induced cGAS-STING signaling only partially through the inhibition of K⁺ efflux *in vitro*. However, whether this is the case *in vivo* is unknown and other mechanisms need to be further explored.

In addition, previous studies have shown that AIM2 inhibition is an effective strategy for improving the efficacy of melanoma immunotherapy by promoting STING-induced type I IFN secretion, as well as limiting IL-1 β and IL-18 production (Fukuda et al., 2021). Our study further supports this previous study and provides a conceptual advance by interrogating the role of GSDMD directly and providing direct evidence that GSDMD specifically in APCs regulates the anti-tumor response by targeting cGAS-STING signaling. Moreover, our study outlines in detail the regulatory framework in which GSDMD deficiency mediates enhanced ISG signaling and CD8⁺ T cell anti-tumor immunity by affecting antigen presentation, which has not been previously studied. Additionally, we found that GSDMD activation in tumor APCs is partially dependent on the AIM2 inflammasome, indicating other existing upstream signaling events are involved in the activation of GSDMD and highlights a more prominent role for inhibiting GSDMD as a therapeutic strategy for promoting anti-tumor immunity. Meanwhile, we found that DMF, an approved drug for the management of relapsing-remitting multiple sclerosis, suppresses the cleavage and activation of GSDMD (Humphries et al., 2020; Narapureddy and Dubey, 2019), and significantly improves anti-tumor immunity in combination with PD-L1 antibody treatment. Therefore, our findings provide an optimistic opportunity for the anti-tumor clinical transformation therapy through targeting GSDMD.

Unlike other gasdermin proteins, GSDMD is also highly expressed in many tumor cells, which suggests that tumor cells may also adopt a strategy of elevated GSDMD expression to suppress anti-tumor immunity and promote tumor growth. Over-expression of GSDMD in tumor cells, significantly reduced the anti-tumor effects of PD-L1 blockade. Given that apoptotic signals are abundant in tumor cells and apoptotic caspase-3/7 can rapidly cleave and inactivate GSDMD at posi-

tion D88 (Feng et al., 2019; Kasibhatla and Tseng, 2003), we speculate that GSDMD in tumor cells can only mediate the transient formation of pores, which are not sufficient to mediate loss of plasma membrane integrity and cell death, yet sufficiently suppress cGAS-mediated inflammation. However the nature of tumor intrinsic GSDMD awaits further investigation in future studies.

In summary, we have identified GSDMD as a restriction factor that suppresses CD8⁺ T cell anti-tumor response during cancer immunotherapy. Given that there are currently no good clinical drugs targeting the cGAS-STING pathway, our findings in this study highlight the potential value of developing therapeutic strategies to block GSDMD-mediated pyroptosis to enhance cGAS-induced ISG in combination with anti-PD-L1 therapy to promote anti-tumor immunity.

Limitations of the study

Although we demonstrated that GSDMD restricts anti-tumor immunity during PD-L1 checkpoint blockade, this study still has limitations. We found that GSDMD attenuates the activation of cGAS-STING signaling following transfer DNA stimulation, primarily dependent on pyroptosis but partially through K⁺ efflux *in vitro*. However, whether this is the case *in vivo* is unknown, and other possible mechanisms that underpin these regulatory effects requires further exploration. Moreover, we found that GSDMD activation in tumor APCs is partially dependent on AIM2 inflammasome, indicating that other unknown upstream signaling events may play a role in activating GSDMD in the TME. These upstream events remain to be explored.

STAR★METHODS

Detailed methods are provided in the online version of this paper and include the following:

- KEY RESOURCES TABLE
- RESOURCE AVAILABILITY
 - Lead contact
 - Materials availability
 - Data and code availability
- EXPERIMENTAL MODEL AND SUBJECT DETAILS
 - Mice
 - Cell lines
 - Tumor induction
- METHOD DETAILS
 - Flow cytometry and myeloid cells sorting
 - Single-cell RNA sequencing
 - Analysis of scRNA-seq data
 - APC cells stimulation *in vitro*
 - BMDMs culture and stimulation
 - Cell death assays
 - Immunoblot analysis
 - Quantitative RT-PCR
 - ELISA
 - Immunofluorescence of tumor tissues
 - Analysis of data from public database
- QUANTIFICATION AND STATISTICAL ANALYSIS

SUPPLEMENTAL INFORMATION

Supplemental information can be found online at <https://doi.org/10.1016/j.celrep.2022.111553>.

ACKNOWLEDGMENTS

We thank Dr. Feng Shao (National Institute of Biological Sciences, Beijing, China) for kindly providing *Gsdmd*^{−/−} mice. We also thank Dr. Zhengfan Jiang (Peking University, Beijing, China) and Dr. Jiawei Zhou (Institute of Neuroscience, Chinese Academy of Sciences) for kindly providing *cGas*^{−/−} mice and *Cx3cr1*-Cre mice, respectively. We thank Dr. Chenqi Xu (Institute of Biochemistry and Cell Biology, Chinese Academy of Sciences) for B16F10 and MC38 cells. We thank Dr. Xiaoming Wang (School of Basic Medical Science, Nanjing Medical University) for providing MCA205 cells. We thank Dr. Hongliang Xin (Nanjing Medical University) for providing GL261 cells. This work was supported by the National Natural Science Foundation of China (grants 82070567 and 32270921 to S.Y., grant 32170742 to X.W., grants 81802393 and 81991523 to B.W., grants 81901227 and 82270539 to C.M., grant 82103328 to Y.W., grant 82104146 to S.L., and grant 82204354 to Y.H.), the Start Fund for Specially Appointed Professor of Jiangsu Province (S.Y. and X.W.), the Open Project of State Key Laboratory of Reproductive Medicine of Nanjing Medical University (grant SKLRM-2021B3 to S.Y.), the cultivation project of “High Level Young Scientific and Technological Talents” of Nanjing Medical University (grant NJMURC2020003 to S.Y.), the Start Fund for High-level Talents of Nanjing Medical University (grant NMUR2020009 to X.W.), the Open Project of Chinese Materia Medica First-Class Discipline of Nanjing University of Chinese Medicine (grant 2020YLXK017 to B.W.), the Priority Academic Program Development of Jiangsu Higher Education Institutions (to B.W.), the Natural Science Foundation of Jiangsu Province (grant BK20221352 to B.W.), the Jiangsu Provincial Outstanding Postdoctoral Program (grant 2022ZB419 to Y.H.), and the Postdoctoral Research Funding Project of Gusu School (GSBSHKY202104 to Y.H.).

AUTHOR CONTRIBUTIONS

Y.J., Y.Y., Y.H., R.Y., J.H., Y.L., Y.W., C.M., and S.L. designed and performed the experiments, analyzed the data, and prepared the figures. B.W., X.W., and Z.H. provided key technique mentoring, data analysis, and research resources. B.W. and F.H. contributed to the experimental design and edited the manuscript. S.Y. supervised the project. Y.J., Y.Y., B.W., F.H., and S.Y. wrote the manuscript.

DECLARATION OF INTERESTS

The authors declare no competing interests.

Received: June 6, 2022

Revised: August 23, 2022

Accepted: October 3, 2022

Published: October 25, 2022

REFERENCES

Algazi, A.P., Tsai, K.K., Shoushtari, A.N., Munhoz, R.R., Eroglu, Z., Piulats, J.M., Ott, P.A., Johnson, D.B., Hwang, J., Daud, A.I., et al. (2016). Clinical outcomes in metastatic uveal melanoma treated with PD-1 and PD-L1 antibodies. *Cancer* 122, 3344–3353.

Banerjee, I., Behl, B., Mendonca, M., Shrivastava, G., Russo, A.J., Menoret, A., Ghosh, A., Vella, A.T., Vanaja, S.K., Sarkar, S.N., et al. (2018). Gasdermin D restrains type I interferon response to cytosolic DNA by disrupting ionic homeostasis. *Immunity* 49, 413–426.e5. e415.

Barbie, D.A., Tamayo, P., Boehm, J.S., Kim, S.Y., Moody, S.E., Dunn, I.F., Schinzel, A.C., Sandy, P., Meylan, E., Scholl, C., et al. (2009). Systematic RNA interference reveals that oncogenic KRAS-driven cancers require TBK1. *Nature* 462, 108–112.

Bergsbaken, T., Fink, S.L., and Cookson, B.T. (2009). Pyroptosis: host cell death and inflammation. *Nat. Rev. Microbiol.* 7, 99–109.

Best, J.A., Blair, D.A., Knell, J., Yang, E., Mayya, V., Doedens, A., Dustin, M.L., and Goldrath, A.W.; Immunological Genome Project Consortium (2013). Transcriptional insights into the CD8+ T cell response to infection and memory T cell formation. *Nat. Immunol.* 14, 404–412.

de Mingo Pulido, Á., Hänggi, K., Celias, D.P., Gardner, A., Li, J., Batista-Bitten-court, B., Mohamed, E., Trillo-Tinoco, J., Osunmakinde, O., Peña, R., et al. (2021). The inhibitory receptor TIM-3 limits activation of the cGAS-STING pathway in intra-tumoral dendritic cells by suppressing extracellular DNA uptake. *Immunity* 54, 1154–1167.e7. e1157.

Dixon, K.O., Tabaka, M., Schramm, M.A., Xiao, S., Tang, R., Dionne, D., Anderson, A.C., Rozenblatt-Rosen, O., Regev, A., and Kuchroo, V.K. (2021). TIM-3 restrains anti-tumour immunity by regulating inflammasome activation. *Nature* 595, 101–106.

Dobin, A., Davis, C.A., Schlesinger, F., Drenkow, J., Zaleski, C., Jha, S., Batut, P., Chaisson, M., and Gingeras, T.R. (2013). STAR: ultrafast universal RNA-seq aligner. *Bioinformatics* 29, 15–21.

Evavold, C.L., Hafner-Bratkovič, I., Devant, P., D’Andrea, J.M., Ngwa, E.M., Borsic, E., Doench, J.G., LaFleur, M.W., Sharpe, A.H., Thiagarajah, J.R., and Kagan, J.C. (2021). Control of gasdermin D oligomerization and pyroptosis by the Ragulator-Rag-mTORC1 pathway. *Cell* 184, 4495–4511.e19. e4419.

Farhood, B., Najafi, M., and Mortezaee, K. (2019). CD8+ cytotoxic T lymphocytes in cancer immunotherapy: a review. *J. Cell. Physiol.* 234, 8509–8521.

Feng, M., Jiang, W., Kim, B.Y.S., Zhang, C.C., Fu, Y.-X., and Weissman, I.L. (2019). Phagocytosis checkpoints as new targets for cancer immunotherapy. *Nat. Rev. Cancer* 19, 568–586.

Fu, C., and Jiang, A. (2018). Dendritic cells and CD8 T cell immunity in tumor microenvironment. *Front. Immunol.* 9, 3059.

Fukuda, K., Okamura, K., Riding, R.L., Fan, X., Afshari, K., Haddadi, N.-S., McCauley, S.M., Guney, M.H., Luban, J., Funakoshi, T., et al. (2021). AIM2 regulates anti-tumor immunity and is a viable therapeutic target for melanoma. *J. Exp. Med.* 218, e20200962.

Gabrilovich, D.I. (2017). Myeloid-derived suppressor cells. *Cancer Immunol. Res.* 5, 3–8.

Gobin, S.J., van Zutphen, M., Woltman, A.M., and van den Elsen, P.J. (1999). Transactivation of classical and nonclassical HLA class I genes through the IFN-stimulated response element. *J. Immunol.* 163, 1428–1434.

Grivennikov, S.I., Greten, F.R., and Karin, M. (2010). Immunity, inflammation, and cancer. *Cell* 140, 883–899.

Han, C., Godfrey, V., Liu, Z., Han, Y., Liu, L., Peng, H., Weichselbaum, R.R., Zaki, H., and Fu, Y.-X. (2021). The AIM2 and NLRP3 inflammasomes trigger IL-1-mediated antitumor effects during radiation. *Sci. Immunol.* 6, eabc6998.

Humphries, F., Shmuel-Galia, L., Ketelut-Carneiro, N., Li, S., Wang, B., Nemmara, V.V., Wilson, R., Jiang, Z., Khalighinejad, F., Muneeruddin, K., et al. (2020). Succination inactivates gasdermin D and blocks pyroptosis. *Science* 369, 1633–1637.

Inoue, H., and Tani, K. (2014). Multimodal immunogenic cancer cell death as a consequence of anticancer cytotoxic treatments. *Cell Death Differ.* 21, 39–49.

Jin, S., Guerrero-Juarez, C.F., Zhang, L., Chang, I., Ramos, R., Kuan, C.-H., Myung, P., Plikus, M.V., and Nie, Q. (2021). Inference and analysis of cell-cell communication using CellChat. *Nat. Commun.* 12, 1088–1120.

Kashyap, D., Tuli, H.S., Sak, K., Garg, V.K., Goel, N., Punia, S., and Chaudhary, A. (2019). Role of reactive oxygen species in cancer progression. *Curr. Pharmacol. Rep.* 5, 79–86.

Kasibhatla, S., and Tseng, B. (2003). Why target apoptosis in cancer treatment? *Mol. Cancer Ther.* 2, 573–580.

Le Tourneau, C., Hoimes, C., Zarwan, C., Wong, D.J., Bauer, S., Claus, R., Wermke, M., Hariharan, S., von Heydebreck, A., Kasturi, V., et al. (2018). Avelumab in patients with previously treated metastatic adrenocortical carcinoma: phase 1b results from the JAVELIN solid tumor trial. *J. Immunother. Cancer* 6, 111–119.

- Li, S., Wu, Y., Yang, D., Wu, C., Ma, C., Liu, X., Moynagh, P.N., Wang, B., Hu, G., and Yang, S. (2019). Gasdermin D in peripheral myeloid cells drives neuroinflammation in experimental autoimmune encephalomyelitis. *J. Exp. Med.* 216, 2562–2581.
- Liu, X., Zhang, Z., Ruan, J., Pan, Y., Magupalli, V.G., Wu, H., and Lieberman, J. (2016). Inflammasome-activated gasdermin D causes pyroptosis by forming membrane pores. *Nature* 535, 153–158.
- Ma, C., Yang, D., Wang, B., Wu, C., Wu, Y., Li, S., Liu, X., Lassen, K., Dai, L., and Yang, S. (2020). Gasdermin D in macrophages restrains colitis by controlling cGAS-mediated inflammation. *Sci. Adv.* 6, eaaz6717.
- Maier, B., Leader, A.M., Chen, S.T., Tung, N., Chang, C., LeBerichel, J., Chudnovskiy, A., Maskey, S., Walker, L., Finnigan, J.P., et al. (2020). A conserved dendritic-cell regulatory program limits antitumor immunity. *Nature* 580, 257–262.
- Maimela, N.R., Liu, S., and Zhang, Y. (2019). Fates of CD8+ T cells in tumor microenvironment. *Comput. Struct. Biotechnol. J.* 17, 1–13.
- McGinnis, C.S., Murrow, L.M., and Gartner, Z.J. (2019). DoubletFinder: doublet detection in single-cell RNA sequencing data using artificial nearest neighbors. *Cell Syst.* 8, 329–337.e4. e324.
- Miller, B.C., Sen, D.R., Al Abosy, R., Bi, K., Virkud, Y.V., LaFleur, M.W., Yates, K.B., Lako, A., Felt, K., Naik, G.S., et al. (2019). Subsets of exhausted CD8+ T cells differentially mediate tumor control and respond to checkpoint blockade. *Nat. Immunol.* 20, 326–336.
- Movahedi, K., Laoui, D., Gysemans, C., Baeten, M., Stangé, G., Van den Bossche, J., Mack, M., Pipeleers, D., Van Ginderachter, J.A., In't Veld, P., and De Baetselier, P. (2010). Different tumor microenvironments contain functionally distinct subsets of macrophages derived from Ly6C (high) monocytes. *Cancer Res.* 70, 5728–5739.
- Nancy, P., and Erlebacher, A. (2014). T cell behavior at the maternal-fetal interface. *Int. J. Dev. Biol.* 58, 189–198.
- Narapureddy, B., and Dubey, D. (2019). Clinical evaluation of dimethyl fumarate for the treatment of relapsing-remitting multiple sclerosis: efficacy, safety, patient experience and adherence. *Patient Prefer. Adherence* 13, 1655–1666.
- Norian, L.A., Rodriguez, P.C., O'Mara, L.A., Zabaleta, J., Ochoa, A.C., Cella, M., and Allen, P.M. (2009). Tumor-infiltrating regulatory dendritic cells inhibit CD8+ T cell function via L-arginine metabolism. *Cancer Res.* 69, 3086–3094.
- Rathinam, V.A.K., Vanaja, S.K., and Fitzgerald, K.A. (2012). Regulation of inflammasome signaling. *Nat. Immunol.* 13, 333–342.
- Schroder, K., and Tschopp, J. (2010). The inflammasomes. *cell* 140, 821–832.
- Tang, Z., Kang, B., Li, C., Chen, T., and Zhang, Z. (2019). GEPIA2: an enhanced web server for large-scale expression profiling and interactive analysis. *Nucleic Acids Res.* 47, W556–W560.
- Thommen, D.S., Koelzer, V.H., Herzig, P., Roller, A., Trefny, M., Dimeloe, S., Kiialainen, A., Hanhart, J., Schill, C., Hess, C., et al. (2018). A transcriptionally and functionally distinct PD-1+ CD8+ T cell pool with predictive potential in non-small-cell lung cancer treated with PD-1 blockade. *Nat. Med.* 24, 994–1004.
- Tu, S., Bhagat, G., Cui, G., Takaishi, S., Kurt-Jones, E.A., Rickman, B., Betz, K.S., Penz-Oesterreicher, M., Bjorkdahl, O., Fox, J.G., and Wang, T.C. (2008). Overexpression of interleukin-1 β induces gastric inflammation and cancer and mobilizes myeloid-derived suppressor cells in mice. *Cancer Cell* 14, 408–419.
- Van Deventer, H.W., Burgents, J.E., Wu, Q.P., Woodford, R.-M.T., Brickey, W.J., Allen, I.C., McElvania-Tekippe, E., Serody, J.S., and Ting, J.P.-Y. (2010). The inflammasome component NLRP3 impairs antitumor vaccine by enhancing the accumulation of tumor-associated myeloid-derived suppressor cells. *Cancer Res.* 70, 10161–10169.
- Wang, H., Hu, S., Chen, X., Shi, H., Chen, C., Sun, L., and Chen, Z.J. (2017). cGAS is essential for the antitumor effect of immune checkpoint blockade. *Proc. Natl. Acad. Sci. USA* 114, 1637–1642.
- Wang, X., Guo, G., Guan, H., Yu, Y., Lu, J., and Yu, J. (2019). Challenges and potential of PD-1/PD-L1 checkpoint blockade immunotherapy for glioblastoma. *J. Exp. Clin. Cancer Res.* 38, 1–13.
- Wherry, E.J., and Kurachi, M. (2015). Molecular and cellular insights into T cell exhaustion. *Nat. Rev. Immunol.* 15, 486–499.
- Xia, P., Wang, S., Gao, P., Gao, G., and Fan, Z. (2016). DNA sensor cGAS-mediated immune recognition. *Protein Cell* 7, 777–791.
- Yang, X., Zhang, X., Fu, M.L., Weichselbaum, R.R., Gajewski, T.F., Guo, Y., and Fu, Y.-X. (2014). Targeting the tumor microenvironment with interferon- β bridges innate and adaptive immune responses. *Cancer Cell* 25, 37–48.
- Zhang, Y., and Zhang, Z. (2020). The history and advances in cancer immunotherapy: understanding the characteristics of tumor-infiltrating immune cells and their therapeutic implications. *Cell. Mol. Immunol.* 17, 807–821.
- Zhang, Z., Zhang, Y., Xia, S., Kong, Q., Li, S., Liu, X., Junqueira, C., Meza-Sosa, K.F., Mok, T.M.Y., Ansara, J., et al. (2020). Gasdermin E suppresses tumour growth by activating anti-tumour immunity. *Nature* 579, 415–420.
- Zhou, Z., He, H., Wang, K., Shi, X., Wang, Y., Su, Y., Wang, Y., Li, D., Liu, W., Zhang, Y., et al. (2020). Granzyme A from cytotoxic lymphocytes cleaves GSDMB to trigger pyroptosis in target cells. *Science* 368, eaaz7548.
- Zitvogel, L., Kepp, O., Galluzzi, L., and Kroemer, G. (2012). Inflammasomes in carcinogenesis and anticancer immune responses. *Nat. Immunol.* 13, 343–351.

STAR★METHODS

KEY RESOURCES TABLE

REAGENT or RESOURCE	SOURCE	IDENTIFIER
Antibodies		
CD45-AF700	eBioscience	Cat# 56-0451-82; RRID: AB_891454
CD11b-FITC	eBioscience	Cat# RM2801; RRID: AB_10373563
CD11c-PE	eBioscience	Cat# 12-0114-82; RRID: AB_465552
F4/80-APC	eBioscience	Cat# 17-4801-82; RRID: AB_2784648
Gr-1-PerCP-Cyanine5.5	eBioscience	Cat# 45-5931-80; RRID: AB_906247
CD4-FITC	eBioscience	Cat# 11-0041-82; RRID: AB_464892
CD8-APC-Cyanine7	Biolegend	Cat# 100714; RRID: AB_312752
CD19-APC	eBioscience	Cat# 17-0193-80; RRID: AB_1659678
NK1.1-PE-Cyanine7	eBioscience	Cat# 25-5941-81; RRID: AB_469664
PD-1-APC	eBioscience	Cat# 17-9985-82; RRID: AB_11149358
TIM-3-PE-Cyanine7	eBioscience	Cat# 25-5870-80; RRID: AB_2573482
Tcrβ- eFluor 450	eBioscience	Cat# 48-5961-80; RRID: AB_11062012
B220-PerCP-Cyanine5.5	eBioscience	Cat# 45-0452-82; RRID: AB_1107006
TER119-PerCP-Cyanine5.5	eBioscience	Cat# 45-5921-82; RRID: AB_925765
IFN-γ-PerCP-Cyanine5.5	eBioscience	Cat# 45-7311-82; RRID: AB_1107020
Ki-67-APC	eBioscience	Cat# 17-5698-82; RRID: AB_2688057
TNF-α-APC	eBioscience	Cat# 17-7321-82; RRID: AB_469508
CD16/CD32	eBioscience	Cat# 14-0161-85; RRID: AB_467134
FOXP3-APC	eBioscience	Cat# 17-5773-80; RRID: AB_469456
MHC II-APC-Cyanine7	Biolegend	Cat# 107627; RRID: AB_1659252
T-bet-BV421	Biolegend	Cat# 644815; RRID: AB_10896427
TIGIT-BV421	BDscience	Cat# 565270; RRID: AB_2688007
Tyrp1-FITC	ZXBio	Cat# TA99; RRID: AB_2922427
Tcf1-APC	Cell Signaling Technology	Cat# 37636; RRID: AB_2922379
p-IRF3-S396	Cell Signaling Technology	Cat# 4947; RRID: AB_823547
p-TBK1	Cell Signaling Technology	Cat# 5483s; RRID: AB_10693472
GSDMD (For IF)	Abcam	Cat# ab219800; RRID: AB_2888940
GSDMD (For WB)	Abcam	Cat# ab209845; RRID: AB_2783550
F4/80	eBioscience	Cat# 14-4801-82; RRID: AB_467558
CD3e	Biorad	Cat# MCA1477; RRID: AB_321245
CD11b	Biolegend	Cat# 101201; RRID: AB_312784
CD11c	Biolegend	Cat# 117314; RRID: AB_492850
PD-L1	Proteintech	Cat# 28076-1-AP; RRID: AB_2881052
Chemicals, peptides, and recombinant proteins		
Percoll	GE Healthcare	Cat# 17-0891-09
PMA	Multi Sciences	Cat# CS0001
Ionomycin	Multi Sciences	Cat# CS0002
BFA	eBioscience	Cat# 00-4506-51
Cytofix/Cytoperm kit	eBioscience	Cat# 88-8824-00
Anti-PD-L1	BioXcell	Cat# BE0101
OXA	Selleck	Cat# s1224
Dimethyl fumarate	MedChemExpress	Cat# HY-17363
AZD2014	MedChemExpress	Cat# HY-15247

(Continued on next page)

Continued

REAGENT or RESOURCE	SOURCE	IDENTIFIER
Critical commercial assays		
Single Cell Sequence Specific Amplification Kit	Vazyme	Cat# P621-01
FAM-FLICA™ Caspase-1 Assay Kit	ImmunoChemistry Technologies	Cat# 98
Hieff qPCR SYBR Green Master Mix	Yeasen	Cat# 11201ES03
LDH Cytotoxicity Assay Kit	Beyotime	Cat# C0017
Mouse TNF-alpha DuoSet ELISA	R&D Systems	Cat# DY410
IFN gamma Mouse Uncoated ELISA Kit	Invitrogen	Cat# 88-7314-82
Mouse IL-1 beta/IL-1F2 DuoSet ELISA	R&D Systems	Cat# DY401
Mouse IL-18 ELISA Kit	Multi Sciences	Cat# EK218
Deposited data		
Single-cell RNA sequencing data	NCBI Gene Expression Omnibus	GSE198550
Experimental models: Cell lines		
B16F10 cells	Dr. Chenqi Xu, Institute of Biochemistry and Cell Biology, Chinese Academy of Sciences	N/A
MCA205 cells	Dr. Xiaoming Wang, Nanjing Medical University, China	N/A
MC38 cells	Dr. Chenqi Xu, Institute of Biochemistry and Cell Biology, Chinese Academy of Sciences	N/A
GL261 cells	Hongliang Xin, Nanjing Medical University, China	N/A
Experimental models: Organisms/strains		
Mouse: C57BL/6J	The Jackson Laboratory	Stock No: 000664
Mouse: <i>Gsdmd</i> ^{-/-}	Dr. Feng Shao, NIBS, China	N/A
Mouse: cGas ^{-/-}	Dr. Zhengfan Jiang, Peking University, China	N/A
Mouse: <i>Gsdmd</i> ^{fl/fl}	Cyagen Biosciences	Product number: S-CKO-14431
Mouse: <i>Cx3cr1</i> -Cre	Dr. Jiawei Zhou, Institute of Neuroscience, Chinese Academy of Sciences	N/A
Mouse: <i>Aim2</i> ^{fl/fl}	Biocytogen Inc	Product number: EGE-CYH-009
Oligonucleotides		
Ifi30 F- CCTGGTCTCCGATCCTACCAT R- TTGCAGGTGGTTGTCCTT	This manuscript	N/A
Sting1 F- GGTCAACGCTCCAAATATGTAG R- CAGTAGTCCAAGTTCGTGCGA	This manuscript	N/A
Oasl1 F- CAGGAGCTGTACGGCTTCC R- CCTACCTTGAGTACCTTGAGCAC	This manuscript	N/A
Ifnb F- CCCTATGGAGATGA CGGAGA R- CCCAGTGCTGGAGAAATTGT	This manuscript	N/A
Gapdh F- TGGATTGGACGCATTGGTC R- TTTGCACTGGTACGTGTTGAT	This manuscript	N/A
Recombinant DNA		
pLV-EF1a-IRES-GSDMD	This paper	N/A
pLKO.1-Puro-TRC-GSDMD	This paper	N/A
Software and Algorithms		
FlowJo Software (version 10.5.3)	FlowJo	https://www.flowjo.com/

(Continued on next page)

Continued

REAGENT or RESOURCE	SOURCE	IDENTIFIER
GraphPad Prism 8.0 or 9.0	GraphPad Software	https://www.graphpad.com
ImageJ 1.49V	ImageJ	https://imagej.nih.gov
Other		
Fixable Viability Dye-eFluor 506	eBioscience	Cat# 65-0866-14

RESOURCE AVAILABILITY

Lead contact

Further information and requests for resources and reagents should be directed to and will be fulfilled by the Lead Contact, Shuo Yang (shuoyang@njmu.edu.cn)

Materials availability

This study did not generate new unique reagents.

Data and code availability

- Single-cell RNA sequencing data generated in this study have been deposited in Gene Expression Omnibus (GEO) under the accession number: GSE198550. To review the GEO accession GSE198550: Go to <https://www.ncbi.nlm.nih.gov/geo/query/acc.cgi?acc=GSE198550>; Enter token ghzuwsklbuhfgd into the box.
- This paper does not report original code.
- Any additional information required to reanalyze the data reported in this paper is available from the [lead contact](#) upon request.

EXPERIMENTAL MODEL AND SUBJECT DETAILS

Mice

All mice were of the species *Mus musculus* (C57BL/6). All experiments were performed using 8-12week male mice. The *Gsdmd*^{-/-} mice were provided by Dr. Feng Shao (National Institute of Biological Sciences, Beijing, China). *cGas*^{-/-} mice were provided by Dr. Zhengfan Jiang (Peking University, Beijing, China). *Gsdmd*^{-/-} mice were crossed with *cGas*^{-/-} to produce *Gsdmd*^{-/-} *cGas*^{-/-} double-knockout mice. The *Gsdmd*^{fl/fl} mice were generated using conditional gene targeting methods as described previously (Li et al., 2019) by Cyagen Biosciences (Guangzhou, China) Inc. The *Aim2*^{fl/fl} mice were generated using conditional gene targeting methods by Biocytogen Inc (Beijing, China). *Gsdmd* and *Aim2* floxed mice were crossed with *Cx3cr1*-Cre mice, provided by Dr. Jiawei Zhou (Institute of Neuroscience, Chinese Academy of Sciences), to obtain myeloid cell-conditional knockout mice (*Gsdmd*^{fl/fl} *Cx3cr1*-Cre and *Aim2*^{fl/fl} *Cx3cr1*-Cre). All mice were kept in a barrier facility, and all animal experiments were conducted in accordance with the procedure approved by the Ethical Review Committee for Laboratory Animal Welfare of the Nanjing Medical University.

Cell lines

The C57BL/6-derived melanoma B16F10 cells, provided by Dr. Chenqi Xu (Institute of Biochemistry and Cell Biology, Chinese Academy of Sciences), were maintained at 37 °C with 5% CO₂ in RPMI 1640 medium (WISSENT) supplemented with 10% heat-inactivated fetal calf serum and 1% penicillin and streptomycin. The C57BL/6-derived MCA205 cells, provided by Dr. Xiaoming Wang (School of Basic Medical Science, Nanjing Medical University), were maintained at 37 °C with 5% CO₂ in DMEM supplemented with 10% heat-inactivated fetal calf serum and 1% penicillin and streptomycin. For GSDMD overexpression and knockdown, HEK293T cells were transfected with packaging plasmids (psPAX2 and pMD2.G) and pLV-EF1a-IRES vector (overexpression) and pLKO.1-Puro-TRC vector (knockdown) by PolyJet reagent (SigmaGen) according to the manufacturer's instructions. Virus-containing supernatants were collected 48 h after transfection. B16F10 cells and MCA205 cells were cultured with the virus supernatant for 48 h.

Tumor induction

Age- and sex-matched mice of 8-12week were anaesthetized with 1% (w/v) pentobarbital sodium in 10μl per g mice weight by intraperitoneal injection. Then, 1 × 10⁵ B16F10 cells or 3 × 10⁵ MCA205 cells were subcutaneously injected in 100 μl PBS on the flank. Tumor size and survival were recorded every two days from day 7. Tumor size was determined by caliper measurements and calculated by length × width × width /2. Mice bearing tumor with a size that was larger than 1500 mm³ were euthanized. In some experiments, mice were treated with anti-PDL1 at a dose of 200 μg on days 4 and 8 after tumor implantations, oxaliplatin (OXA) at a dose of 5mg/kg on days 7, 11, 15 and 19 days, DMF and AZD2014 at a dose of 10mg/kg every day after tumor implantations.

METHOD DETAILS

Flow cytometry and myeloid cells sorting

In indicated days, tumor tissues were weighed, cut into pieces and suspended with 10 ml tumor digestion buffer (2% FBS, 0.5 mg/ml collagenase IV and 100U/ml DNase I in RPMI medium). After digested for 45 minutes at 37°C under agitation (200 rpm) conditions, cell suspension was filtered using a 70- μ m filter to obtain a single-cell suspension. Immune cells were isolated by density-gradient centrifugation using 40% and 80% Percoll. Then, tumor-infiltrating immune cells were stained using fluorescently labelled antibodies for FACS analysis.

For intracellular staining of IFN- γ and TNF- α , tumor single-cell suspensions were incubated in RPMI medium containing PMA (1:2000), ionomycin (1:1000), and BFA (1:1000) for 4 hours at 37°C. After washing the samples with HBSS, surface proteins were stained, followed by fixation and permeabilization using the Cytofix/Cytoperm kit (eBioscience, cat# 88-8824-00), then staining of intracellular IFN- γ and TNF- α . Caspase-1/11 activity was quantified according to manufacturer's protocol. Briefly, cells were incubated with FAM-FLICA reagent for 30 min at 37°C and cells were washed two times with media to diffuse unbound FLICA. Propidium iodide (PI) was stained 5 min before flow cytometer detection. For antigen-presenting cells sorting, single-cell suspensions were stained with FVD eFluor 506, anti-CD45, anti-tcr β , anti-TER119, anti-B220 and anti-Gr-1. DCs and macrophages (CD45⁺ Lin⁻ (tcr β ⁻ B220⁻ TER119⁻ Gr-1⁻) were sorted on a BD FACSAria.

Single-cell RNA sequencing

The immune cells in tumors were sorted from *GSDMD^{fl/fl} Cx3cr1-Cre* mice and *Cx3cr1-Cre* mice with anti-PD-L1 treatment 14 days after tumor implantations. Single-cell suspensions (1×10^5 cells/ml) with PBS were loaded into microfluidic devices using the Single-ron Matrix® Single Cell Processing System (Singleron). Subsequently, the scRNA-seq libraries were constructed according to the protocol of the GEXSCOPE® Single Cell RNA Library Kits (Singleron). Individual libraries were diluted to 4 nM and pooled for sequencing. At last, libraries were sequenced on Illumina NovaSeq 6000 with 150 bp paired end reads.

Analysis of scRNA-seq data

scRNA-seq data processing

In total, we generated 1.4 billion paired-end Illumina sequencing reads from the prepared scRNA-seq libraries (see above). The raw reads were processed to generate gene expression profiles using an internal pipeline (<https://github.com/singleron-RD/CeleScope>). Briefly, cell barcodes and UMI sequences were extracted after filtering out low-quality reads or reads without poly(T) tails presented in their first ends. Then, adapters and poly(A) tails (i.e., a stretch of 18 A's) were trimmed from the second ends of the filtered reads (cutadapt v1.17), followed by read alignment to the mouse reference genome (mm10) with gene annotation (ensembl v102) using STAR (version 2.7.7a) (Dobin et al., 2013). After UMI deduplication, the numbers of reads mapped to individual genes for every cell barcode were counted (featureCounts v2.0.1) (Nancy and Erlebach, 2014), and the UMI count tables were employed for downstream analysis. Finally, background barcodes and authentic barcodes corresponding to cells were segregated by checking the distribution of total UMI counts for individual cell barcodes. As a result, the processing pipeline recovered 4,874, 4,891, 7,173 and 5,592 cells in each of the four libraries, respectively.

Basic analysis of single-cell RNA-seq data

With the gene-by-cell UMI count matrixes, we first filtered out low quality cells if not satisfied all the following criteria: (i) number of detected genes between 600 and 8000, (ii) number of total UMIs less than 80000, and (iii) percentage of UMIs derived from mitochondrial genes below 10%. We then normalized the UMI counts by library size factors, where the library size factor is equal to the sum of UMIs in each single cell divided by 10000; then log2-transformed the normalized UMI counts. To further remove cell barcodes accommodating possible doublets, we adopted the DoubletFinder algorithm (McGinnis et al., 2019) implemented in the DoubletFinder package (v 2.0.3) with the expected doublet formation 7.5%, and the putative doublets in the data were removed from the downstream analysis. We then merged the expression data from the four libraries (i.e., the samples derived from the *Gsdmd^{fl/fl} Cx3cr1-Cre* mice and *Cx3cr1-Cre* mice, each with two replicates), and repeated the analysis of expression data scaling, HVG detection, PCA computation, cell clustering identification and dimensional reduction using the Seurat (v4.0.0) package. With the *Ptprc* marker (encoding protein CD45), we further removed clusters comprised of non-immune cells and rare cells (that is the distinct clusters each containing less than 1% cells).

Marker gene identification and cluster annotation

In order to characterize and annotate the cell clusters, we applied the function FindMarkers in the Seurat package to identify genes specifically expressed in each cluster. Only genes expressed in more than 25% of the cells in a cluster and with log2-transformed fold-changes on average greater than 0.25 were considered as marker genes. Wilcoxon rank sum tests were used to assess the statistical significance. The top ranked markers of each cluster were shown in the heatmap. Based on the identified markers and our prior knowledge of immune cell types, we manually annotated the cell clusters with particular cell types.

Calculation of gene signature scores

To interpret the differential expression between cells derived from *Gsdmd*^{fl/fl} *Cx3cr1*-Cre mice and *Cx3cr1*-Cre mice with potential cellular functions, we calculated gene signature scores using the single-sample gene set enrichment analysis (ssGSEA) algorithm (Barbie et al., 2009) based on previously defined gene sets. The detailed information of the gene sets used in this study can be found in Table S1.

Cell-cell communication inference

To systematically characterize cellular crosstalk between CD8⁺ T cells and the other cell types, we preformed cell-cell communication inference based on the scRNA-seq data. To achieve this, we adopted the CellChat algorithm (Jin et al., 2021), which scores the communication between different cell types by assessing the averaged expression of ligands, receptors, and their cofactors in each cell type, calculating the ligand-receptor interaction probability with a permutation test, and aggregating the communication strength of various ligand-receptor pairs. We implemented the above process with the CellChat package (version 1.1.3) following its tutorial with default parameters except adjusting the following two parameters: type = "truncatedMean", and trim=0.1 in the function computeCommunProb, in order to investigate the ligand-receptor interactions in a more comprehensive manner. The annotation of ligand-receptor pairs and their cofactors was supplied by CellChatDB (mouse version), which is a manually curated database of literature-supported ligand-receptor interactions in mouse.

APC cells stimulation *in vitro*

APC cells sorting was described above. Cell-free tumor DNA (T-DNA) from B16F10 cells was extracted according to the manufacturer's instruction (Thermo, A29319). The purified cells were cultured in DMEM (Gibco) supplemented with 1% penicillin and streptomycin, and 10% fetal bovine serum (Sigma-Aldrich) and transfected with Lipofectamine 2000 (2 μ l/ml)-complexed T-DNA from B16F10 tumor cells (1 μ g per 10⁶ cells) for 12 hours. The stimulated-cells were analyzed for ISGs by QPCR and p-IRF3 and -TBK1 protein levels by FACS.

BMDMs culture and stimulation

For isolation of BMDMs, tibias and femurs were removed from indicated mice by sterile techniques and the bone marrow was flushed with fresh medium. BMDMs were plated in DMEM supplemented with 10% FBS in the presence of 10% L929 conditioned medium for 6 days at 37 °C in a humidified atmosphere of 5% CO₂. Primary BMDMs were seeded (1.2 \times 10⁶ cells per well) in 12-well plates (NEST Biotechnology) and were grown for 24 h. Cells were then stimulated with T-DNA (1 μ g/ml) for 8 hours.

Cell death assays

Cell death was determined by the lactate dehydrogenase release assay using the Pierce LDH Cytotoxicity Assay Kit (Beyotime) according to the manufacturer's instruction.

Immunoblot analysis

BMDMs, B16F10 cells and MCA205 cells cultured *in vitro* were collected in 1x SDS-PAGE Protein Loading Buffer (Yeast) and boiled for 10 min. Proteins were separated by SDS-polyacrylamide gel electrophoresis and transferred onto nitrocellulose membranes. The membranes were immunoblotted with primary antibodies and proteins detected with appropriate secondary anti-rabbit antibody conjugated to fluorescence. Immunoreactivity was visualized by the Odyssey Imaging System (LI-COR Biosciences).

Quantitative RT-PCR

Tumor tissue RNA was extracted using TRIzol reagent (Life) and subjected to cDNA synthesis. Myeloid cells stimulated *in vitro* RNA extraction and cDNA synthesis were performed by using Single Cell Sequence Specific Amplification Kit (Vazyme). Total RNA of BMDMs was extracted using TRIzol reagent and subjected to complementary DNA synthesis. Reverse transcription products of different samples were amplified by StepOnePlus (Applied Biosystems) using Hieff qPCR SYBR Green Master Mix (Yeast) according to the manufacturer's instructions. All primers were purchased from GenScript.

ELISA

To determine the levels of TNF- α , IFN- γ , IL-1 β and IL-18 protein in the tumor microenvironment, the tumor collected on day 14 after implant was homogenized by mechanic disruption with magnetic beads in PBS buffer with complete protease inhibitors. After centrifugation, the supernatant was collected and measured for levels of TNF- α , IFN- γ , IL-1 β and IL18, according to the manufacturer's instructions.

Immunofluorescence of tumor tissues

Freshly isolated tumor tissues were fixed in Periodate-lysine-paraformaldehyde (PLP) fixative 4°C for overnight, dehydrated, and mounted in paraffin using standard protocols. Material for frozen sections was processed and embedded in OCT (Tissue-Tek; Sakura Finetek) according to standard protocols. Frozen sections were used for con-staining of PD-L1 with Tyrp1 and CD11b, and co-staining of GSDMD with CD11c. Paraffin sections were used for co-staining of GSDMD with CD3e and F4/80. For co-staining of CD11c with GSDMD, frozen sections were blocked and permeabilized in 5% goat serum and 0.1% Triton X-100 in PBS for 1 h and incubated

with primary antibodies diluted in 0.2% Triton X-100 in PBS at 4°C for overnight. Other stainings were according to the standard immunofluorescence protocols. Antibodies including: rabbit anti-GSDMD (1:500), rat anti-F4/80 (1:200), rat anti-CD3e (1:200), rat anti-CD11b (1:200), rabbit anti-PD-L1 (1:200), Alexa Fluor647 Armenian Hamster anti CD11c (1:200) and FITC mouse anti-Tyrrp1 (1:200). Secondary antibodies were anti-rabbit goat antibodies conjugated with Alexa 555 (1:600) and anti-rat goat antibodies conjugated with Alexa 488 (1:600). The Images were taken using Zeiss LSM 800 confocal microscope and processed using ImageJ and AdobePhotoshopCS6 software.

Analysis of data from public database

To explore the role of gasdermin members in immune cells related to tumor environment, we analyzed the expression of gasdermin family genes (including *GSDMA*, *GSDMB*, *GSDMC*, *GSDMD*, *DFNA5* (also known as *GSDME*) and *DFNB59*) in immune cells from publicly available gene and protein databases such as ImmGen (<https://www.immgen.org/>) EMBL database (<https://www.ebi.ac.uk/>) and BioGPS (<http://biogps.org/>). We processed whole-transcriptome data from the Cancer Cell Line Encyclopedia (CCLE) data portal (<https://sites.broadinstitute.org/ccle/>) to analyze the expression of gasdermin family members in tumor cells. To explore the correlation between gasdermin family members and immune checkpoints in clinical tumors, we examined the gene expression profiles of pan-cancer clinical data from TCGA databases using the Gene Expression Profiling Interactive Analysis 2 (GEPIA2) platform (<http://gepia2.cancer-pku.cn/>). The immune checkpoint genes include *PDCD1*, *LAG3*, *HAVCR2*, *TIGIT*, *CTLA4*, *CD244* (*PDL1*), *IL10RB*, *IDO1*, *LGALS9*, *ADORA2A*, *PVRL2*, *CD160*, *BTLA*, *CD96*, *CD97*, *CD112R* and *CD200R*. We termed the above immune checkpoint genes as a signature and analyzed the correlation between gasdermin family genes and immune checkpoint signature in both pan-cancer and 33 individual types of cancers. To explore the relationship between the survival rate of patient and gasdermin expression, TCGA database was download from <http://firebrowse.org/>, and Kaplan-Meier plot of overall survival of patients based on gasdermin expression was shown. A log-rank test was used for statistical analysis.

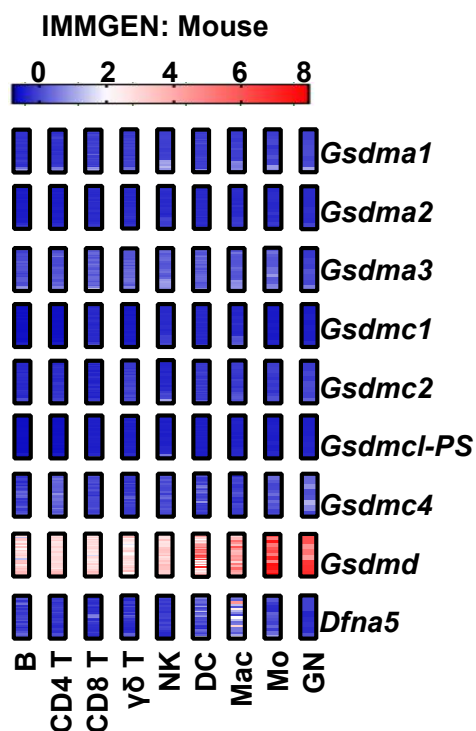
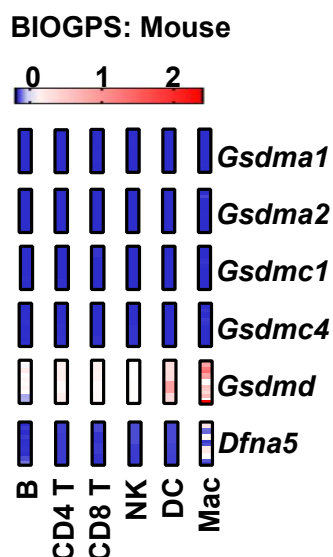
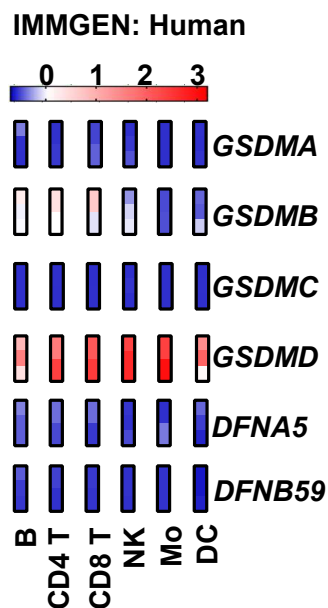
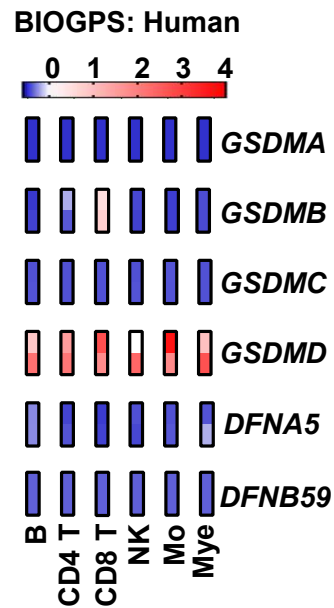
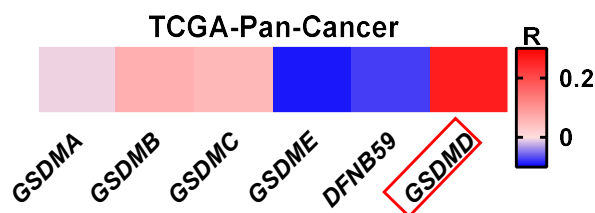
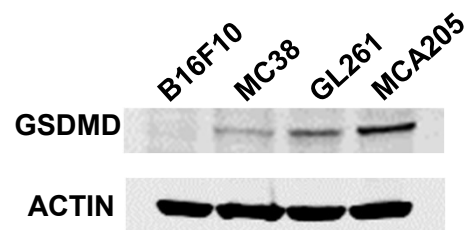
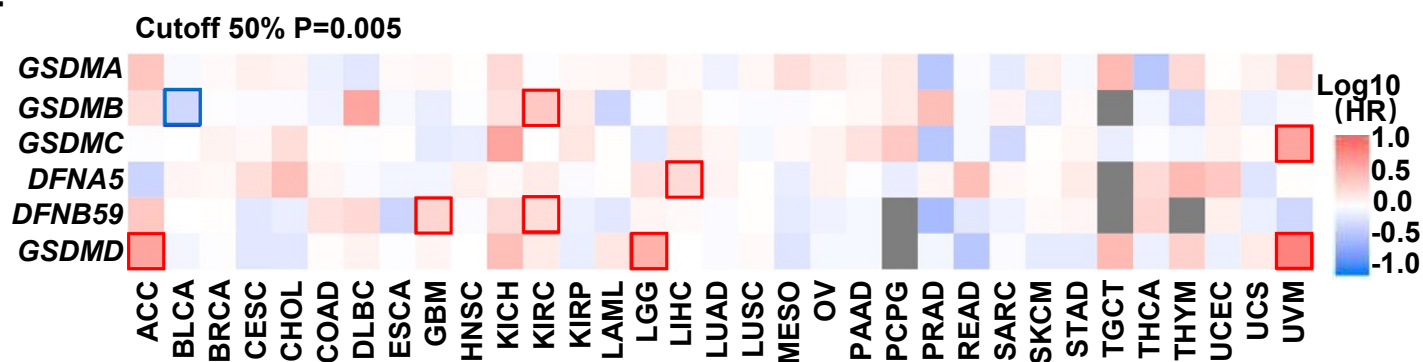
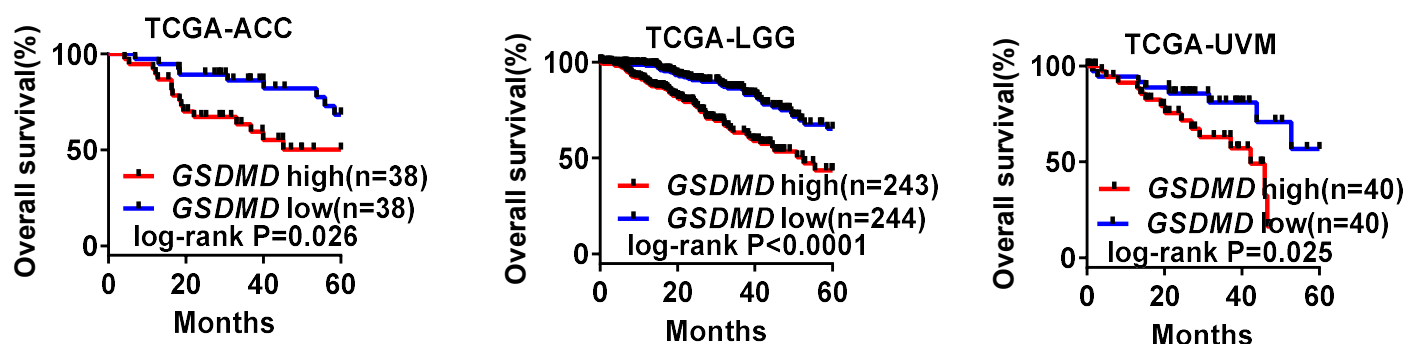
QUANTIFICATION AND STATISTICAL ANALYSIS

Information about statistical details and methods is indicated in the figure legends. Statistical analysis was performed using GraphPad Prism 8.0 or 9.0.

Supplemental information

**Gasdermin D restricts anti-tumor immunity
during PD-L1 checkpoint blockade**

Yuying Jiang, Yongbing Yang, Yingchao Hu, Rui Yang, Jiajia Huang, Yi Liu, Yuqing Wu, Sheng Li, Chunmei Ma, Fiachra Humphries, Bingwei Wang, Xi Wang, Zhibin Hu, and Shuo Yang

A**B****C****D****E****H****F****G**

Supplementary Figure 1. Gasdermin D is highly expressed in myeloid cells and positively correlates with the immune checkpoint signature. Related to Figure 1.

(A) ImmGen data showing the expression of gasdermin family in different immune cells from mouse.

(B) BioGPS data showing the expression of gasdermin family in different immune cells from mouse.

(C) ImmGen data showing the expression of gasdermin family in different immune cells from human.

(D) BioGPS data showing the expression of gasdermin family in different immune cells from human.

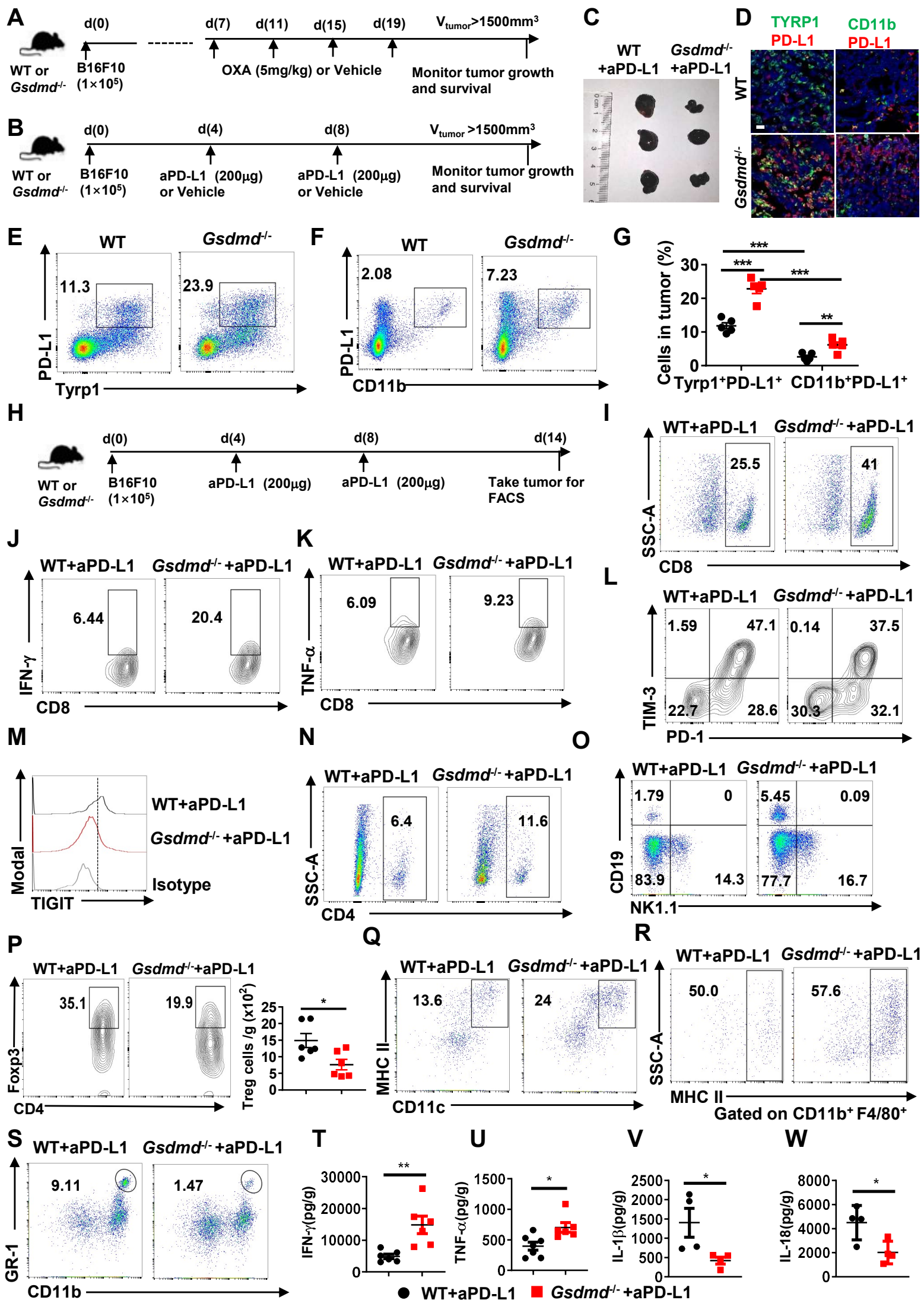
(E) Correlation analysis of gene expression profiles between gasdermin family members and ICs signature from pan-cancer in TCGA database.

(F) Survival map of six human gasdermins from 33 types of tumors using GEPIA2. Gasdermins expression in all tumors from TCGA data were scored, top 50% and low 50% were considered as high and low expression (at cutoff 50%), respectively. The blue square means that the low expression of indicated gene was correlated with poor survival of patients (P value < 0.005), and the red square means that the high expression of indicated gene was correlated with poor survival of patients (P value < 0.005).

(G) Kaplan-Meier plot of overall survival of patients with adrenocortical carcinoma (ACC), low-grade glioma (LGG), and uveal melanoma (UVM) based on *GSDMD* expression levels from TCGA data at cutoff 50%.

(H) Immunoblot analysis of GSDMD expression in different types of tumor cells (B16F10 cells, MC38 cells, GL261 cells and MCA205 cells).

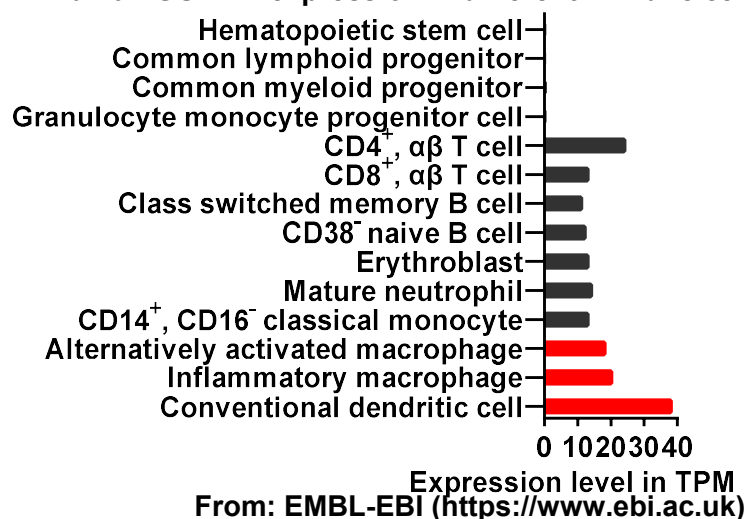
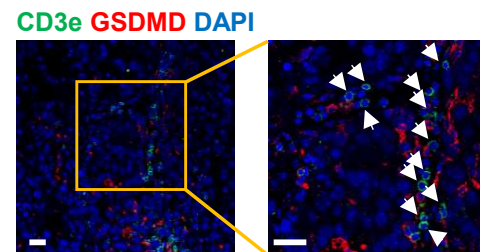
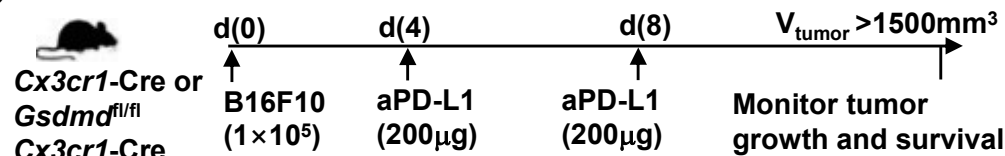
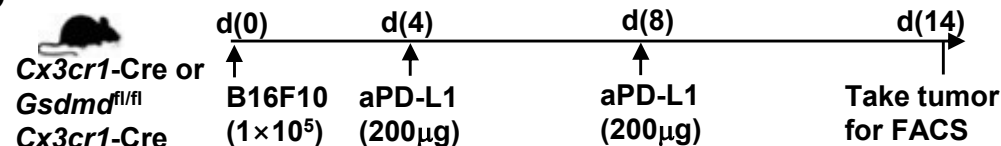
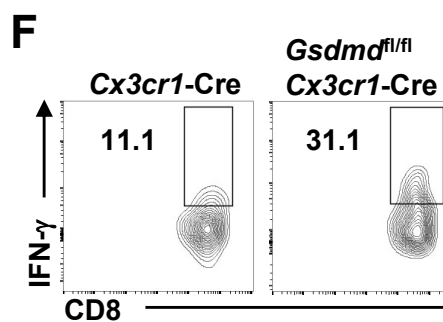
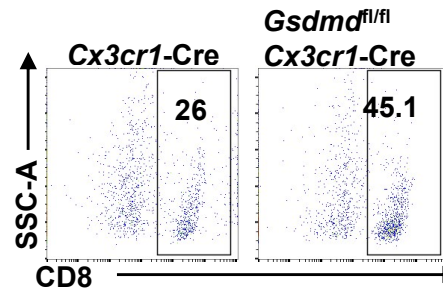
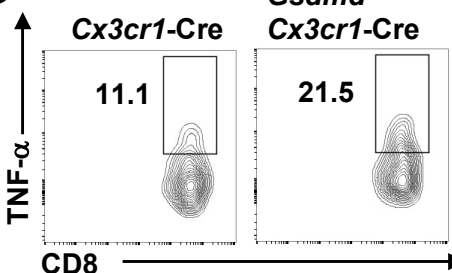
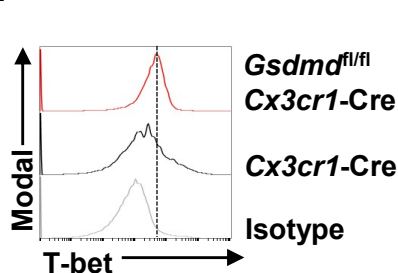
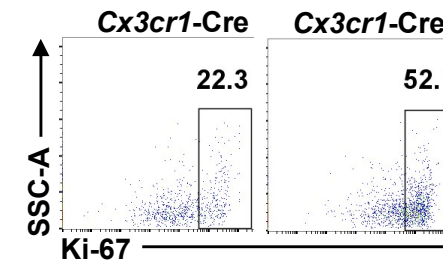
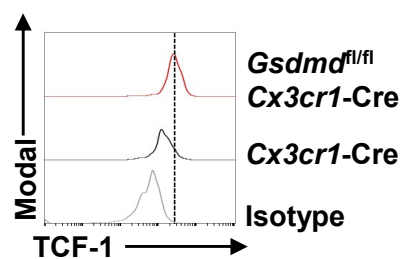
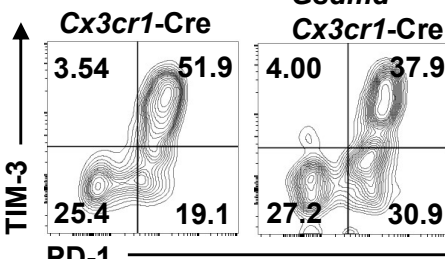
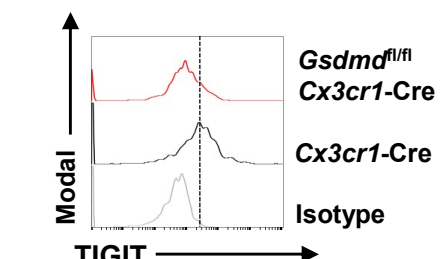
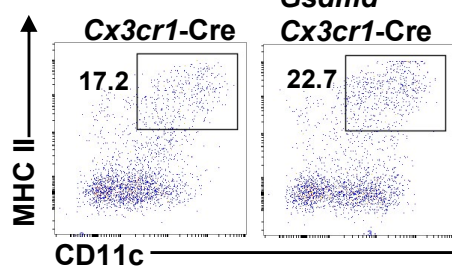
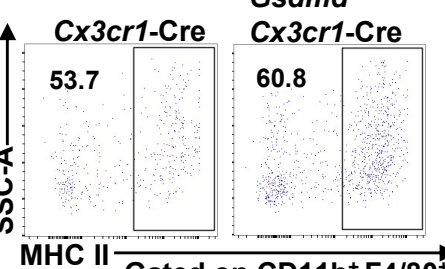
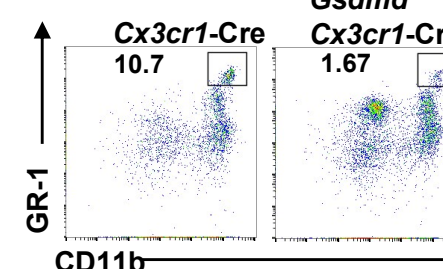
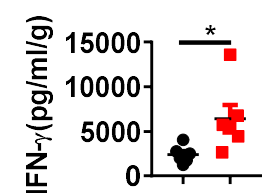
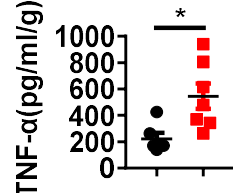
Error bars show mean \pm sem. Log-rank test for (G).



Supplementary Figure 2. GSDMD deficiency enhances antitumor immunity under the treatment of PD-L1 antibody. Related to Figure 1.

- (A) Schematic representation of the experiments in Figure 1G. 1×10^5 B16F10 cells were implanted subcutaneously into WT and *Gsdmd*^{-/-} mice, OXA (5mg/kg) or vehicle were intraperitoneally injected on day 7, 11, 15, 19. Tumor volumes and mice survival were assessed every other day from day 7. Mice were euthanized when tumor volumes exceeded 1500mm³.
- (B) Schematic representation of the experiments in Figure 1H. 1×10^5 B16F10 cells were implanted subcutaneously into WT and *Gsdmd*^{-/-} mice, aPD-L1 (200μg) or vehicle were intraperitoneally injected on day 4, 8. Tumor volumes and mice survival were assessed every other day from day 7. Mice were euthanized when tumor volumes exceeded 1500mm³.
- (C) Photographs of representative tumors in groups of WT and *Gsdmd*^{-/-} mice with aPD-L1 treatment on day 14 after implantation.
- (D) Immunofluorescence staining for PD-L1 (red) and Tyrp1 (green, left) or CD11b (green, right) in tumor tissue from indicated mice. Scale bars, 20 μm.
- (E-G) Tumors were collected from indicated mice on 14 days to analyze PD-L1 co-expression with Tyrp1 or CD11b by FACS.
- (H) Schematic representation of the experiments in Figure 1I-V. 1×10^5 B16F10 cells were implanted subcutaneously into WT and *Gsdmd*^{-/-} mice, aPD-L1 (200μg) or vehicle were intraperitoneally injected on day 4, 8. Tumors were collected on day 14 after implantation.
- (I) Representative flow cytometry plots of CD8⁺ T cells in Figure 1I.
- (J-K) Representative flow cytometry plots of CD8⁺ IFN-γ⁺ (I) and TNF-α⁺ (J) T cells in Figure 1J-M.
- (L) Representative flow cytometry plots of PD-1 and TIM-3 expression of CD8⁺ T cells in Figure 1N-O.
- (M) Representative flow cytometry plots of TIGIT expression in CD8⁺ T cells in Figure 1P.
- (N) Representative flow cytometry plots of CD4⁺ T cells in Figure 1Q.
- (O) Representative flow cytometry plots of CD19⁺ cells and NK1.1⁺ cells in Figure 1r and Figure 1S, respectively.
- (P) Representative flow cytometry plots gated from CD45⁺CD4⁻ (left) and quantitative analysis of Treg number (right) from tumors on day 14.
- (Q-S) Representative flow cytometry plots of DCs (O), MHC II⁺ macrophages (P) and MDSCs (Q) in Figure 1T-V.
- (T-W) WT and *Gsdmd*^{-/-} mice were implanted subcutaneously with B16F10 cells and were treated with PD-L1 on day 4 and day 8. Tumors were collected on day 14 after implantation to assess IFN-γ (T), TNF-α (U), IL-1β (V) and IL-18 (W) protein levels by ELISA.

Data are pooled from two independent experiments for (G, T-W), data are representative of three independent experiments for (D-F, I-S) and data are pooled from three independent experiments for (P). Error bars show mean ± sem. * $P \leq 0.05$, ** $P \leq 0.01$, *** $P \leq 0.001$. Two-tailed unpaired student's *t*-test for (G, P and T-W).

AHuman *GSDMD* expression in different immune cells**B****C****D****E****F****G****H****I****J****K****L****M****N****O****P**

● *Cx3cr1-Cre* + aPD-L1
■ *Gsdmd*^{-/-} *Cx3cr1-Cre* + aPD-L1

Supplementary Figure 3. GSDMD deficiency in APCs enhances antitumor immunity. Related to Figure 2.

(A) EMBL data showing the expression of GSDMD in different human immune cells.

(B) Immunofluorescence staining for GSDMD (red) and CD3 (green) in tumor tissue from WT mice. Scale bars, 20 μ m. The white arrows indicate GSDMD⁻ and CD3e⁺ cells.

(C) Schematic representation of the experiments in Figure 2D-E. 1×10^5 B16F10 cells were implanted subcutaneously into *Cx3cr1*-cre and *Gsdmd^{fl/fl}* *Cx3cr1*-cre mice, aPD-L1 (200 μ g) or vehicle were intraperitoneally injected on day 4, 8. Tumor volumes and mice survival were assessed every other day from day 7. Mice were euthanized when tumor volumes exceeded 1500mm³.

(D) Schematic representation of the experiments in Figure 2F-S. 1×10^5 B16F10 cells were implanted subcutaneously into *Cx3cr1*-cre and *Gsdmd^{fl/fl}* *Cx3cr1*-cre mice, aPD-L1 (200 μ g) or vehicle were intraperitoneally injected on day 4, 8. Tumors were collected on day 14 after implantation.

(E) Representative flow cytometry plots of CD8⁺ T cells in Figure 2F.

(F-G) Representative flow cytometry plots of CD8⁺ IFN- γ ⁺ (F) and TNF- α ⁺ (G) T cells in Figure 1G-J.

(H-J) Representative flow cytometry plots of expression of T-bet (H), Ki-67 (I), Tcf-1 (J) in CD8⁺ T cells in Figure 2K-M.

(K) Representative flow cytometry plots of PD-1 and TIM-3 expression of CD8⁺ T cells in Figure 2N-O.

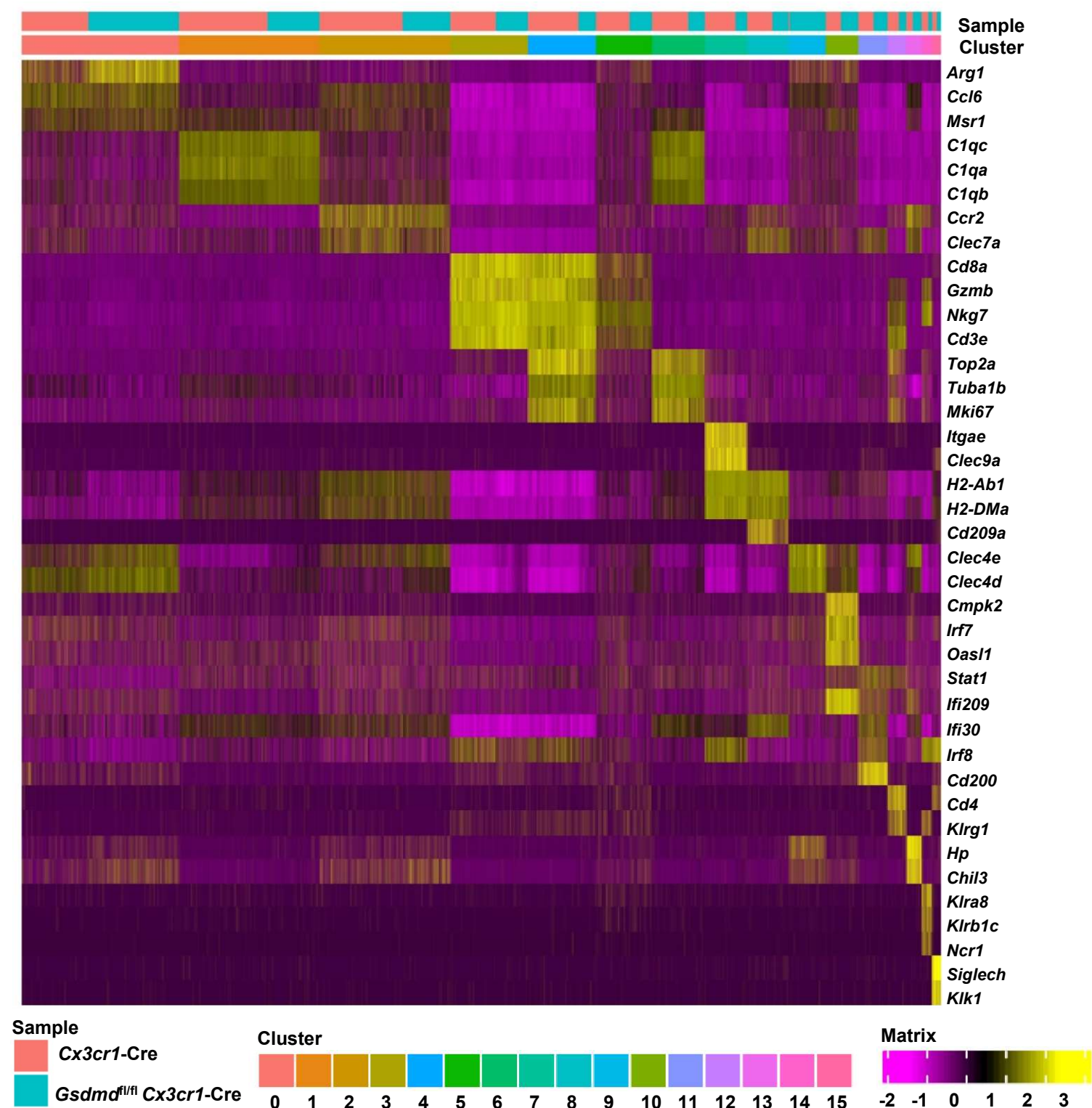
(L) Representative flow cytometry plots of TIGIT expression in CD8⁺ T cells in Figure Figure 2P.

(M-O) Representative flow cytometry plots of DCs (M), MHC II⁺ macrophages (N) and MDSCs (O) in Figure 2Q-S.

(P-Q) *Cx3cr1*-cre and *Gsdmd^{fl/fl}* *Cx3cr1*-cre mice were implanted subcutaneously with B16F10 cells and were treated with aPD-L1 on day 4 and day 8. Tumors were collected on day 14 after implantation to assess IFN- γ (P) and TNF- α (Q) protein levels by ELISA.

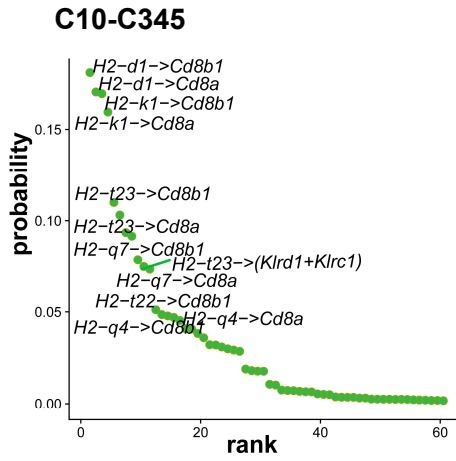
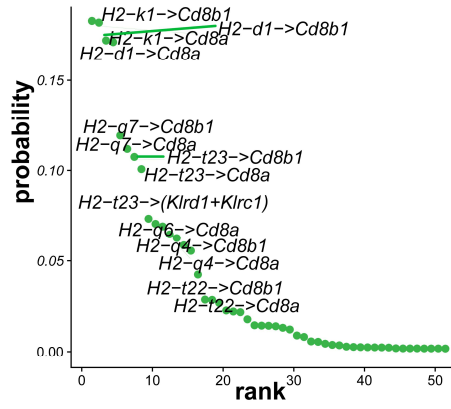
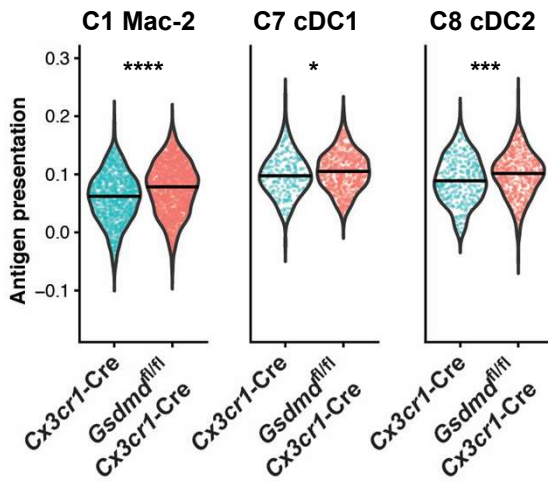
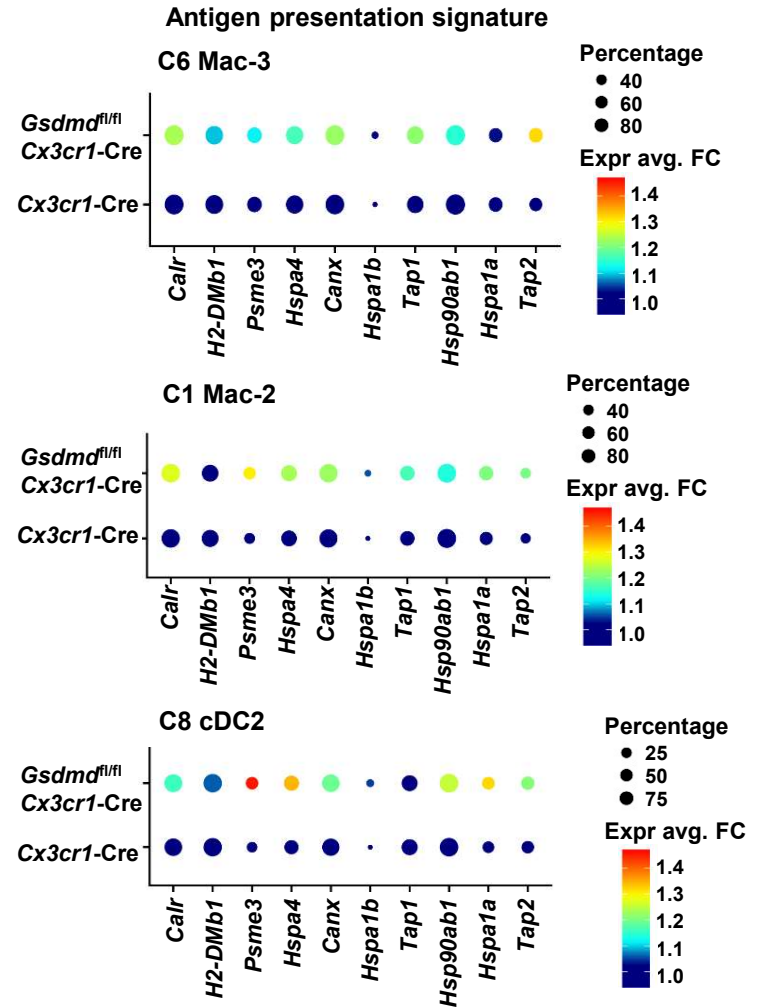
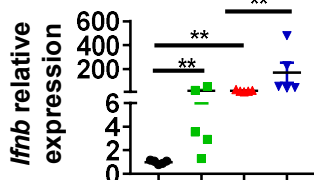
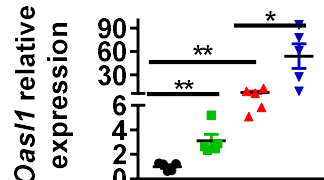
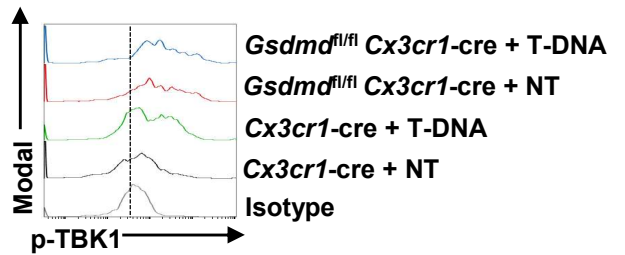
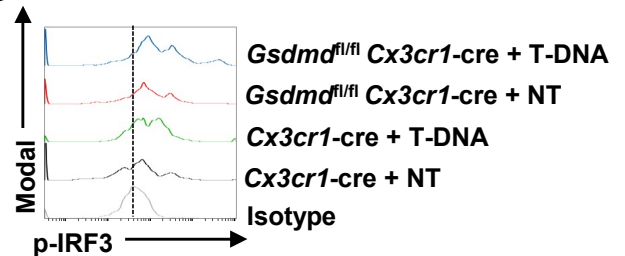
Data are pooled from two independent experiments for (P-Q), and data are representative of three independent experiments for (B, E-O). Error bars show mean \pm sem. * $P \leq 0.05$. Two-tailed unpaired student's *t*-test for (P-Q).

A



Supplementary Figure 4. Gene heatmap of single cell RNA-seq. Related to Figure 3.

(A) Heatmap showing expression of the indicated gene markers for distinct cell-types.

A**C11-C345****B****C****D****E****F****G**

- Cx3cr1-Cre + NT
- Cx3cr1-Cre + T-DNA
- ▲ Gsdmd^{fl/fl} Cx3cr1-Cre + NT
- ▼ Gsdmd^{fl/fl} Cx3cr1-Cre + T-DNA

Supplementary Figure 5. GSDMD deficiency enhances antigen-presentation and ISG expression signatures. Related to Figure 3.

(A) Cell-cell communication inference based on the scRNA-seq data through CellChat algorithm. Probability indicated the scores of communications between different cell types by assessing the averaged expression of ligands, receptors and their cofactors in each cell type.

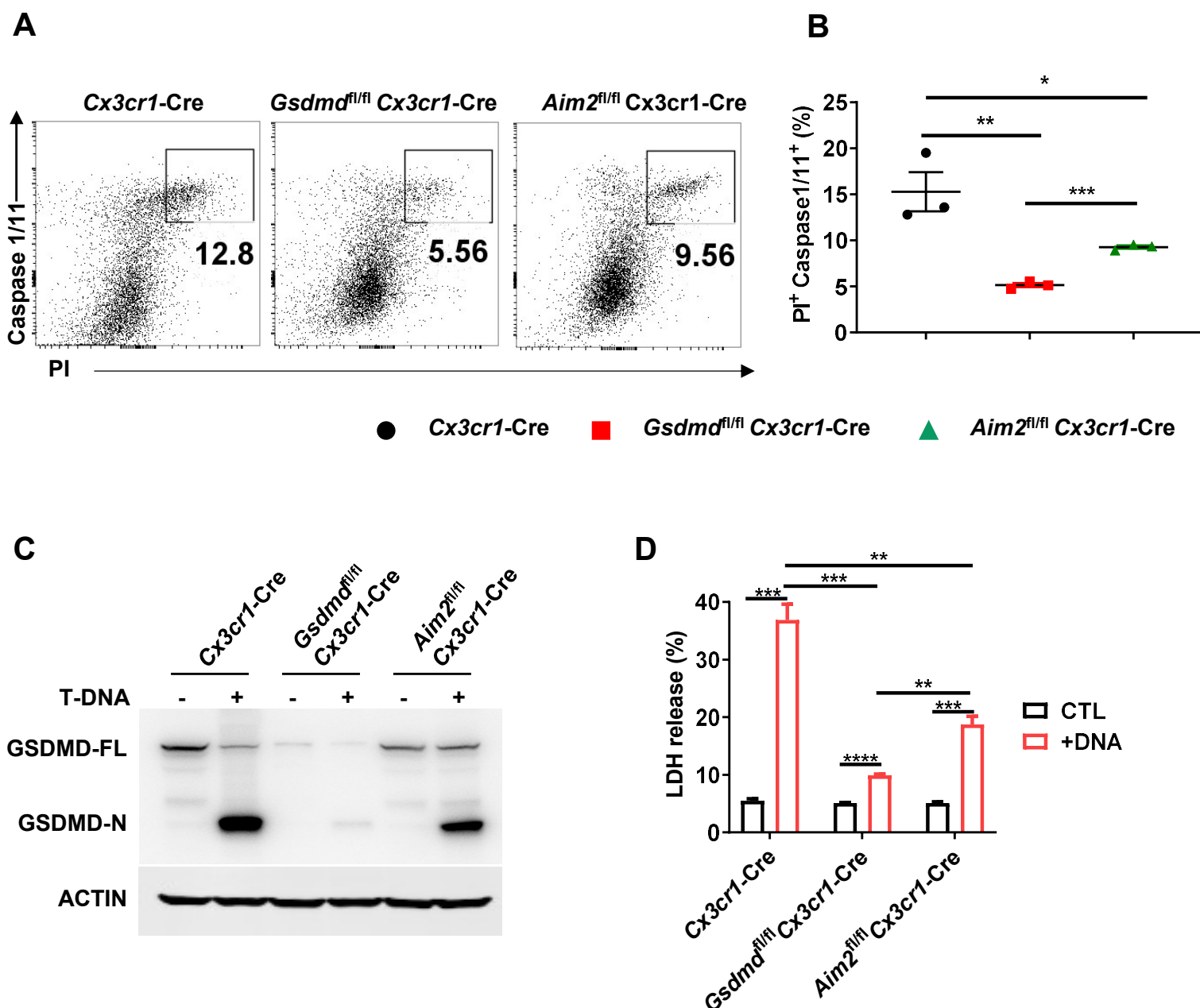
(B) ssGSEA analysis for antigen presentation signature of indicated cell types.

(C) Bubble plot showing the gene expression related to antigen presentation signature of indicated cell type from *Cx3cr1*-cre and *Gsdmd^{fl/fl}* *Cx3cr1*-cre mice.

(D-E) *Cx3cr1*-cre and *Gsdmd^{fl/fl}* *Cx3cr1*-cre mice were implanted subcutaneously with B16F10 cells and intraperitoneal injected with aPD-L1 on day 4 and 8. 14 days later, Lin⁻ CD11b⁺ Gr1⁻ myeloid cells were sorting from tumors and stimulated for 12 hours in vitro by T-DNA from B16F10 cells. Cells were then collected for QPCR analysis of *Ifnb* (D), *Oas1l* (E).

(F-G) Representative flow cytometry plots of p-TBK1(F) and p-IRF3 (G) in Figure 3J-K.

Data are pooled from three independent experiments for (D-E), and data are representative of three independent experiments for (F-G). Error bars show mean \pm sem. * $P \leq 0.05$, ** $P \leq 0.01$, *** $P \leq 0.001$, **** $P \leq 0.0001$. Two-tailed unpaired student's *t*-test for (B, D-E).



Supplementary Figure 6. AIM2 inflammasome is partially responsible for T-DNA-induced GSDMD activation. Related to Figure 3.

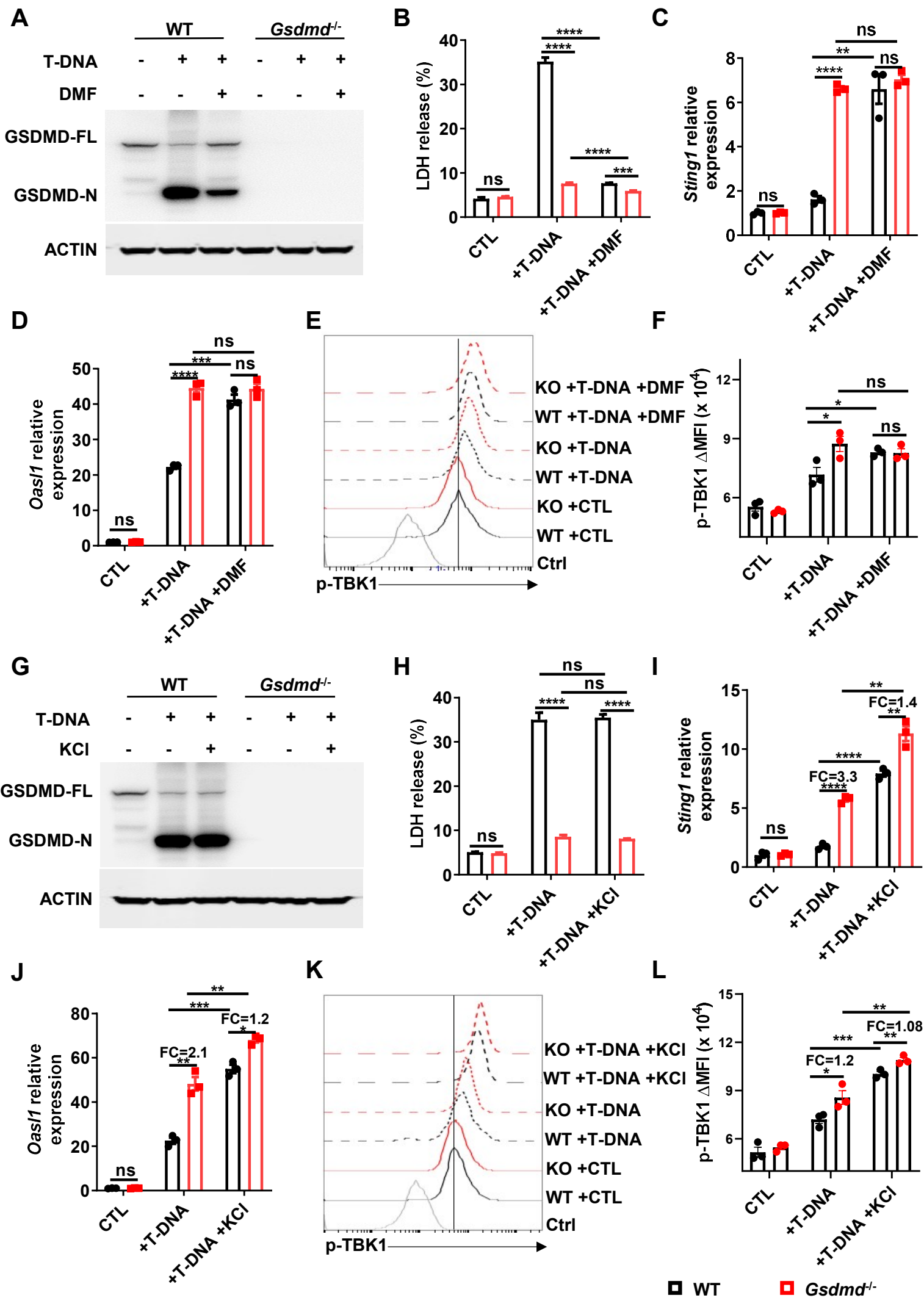
(A) 1×10^5 B16F10 cells were implanted subcutaneously into *Cx3cr1-cre*, *Gsdmd^{fl/fl} Cx3cr1-cre* and *Aim2^{fl/fl} Cx3cr1-cre* mice, aPD-L1 (200 μ g) were intraperitoneally injected on day 4 and day 8. Tumors were collected on day 14 after implantation for flow cytometry analysis of Caspase-1/11⁺PI⁺ APCs gated from CD45⁺Lin⁻CD11b⁺Gr1⁻. Representative flow cytometry plots of Caspase-1/11⁺PI⁺ APCs in tumor.

(B) Flow cytometry quantitative analysis of Caspase-1/11⁺PI⁺ APCs in tumor.

(C) Immunoblot analysis of cell extracts from *Cx3cr1-cre*, *Gsdmd^{fl/fl} Cx3cr1-cre* and *Aim2^{fl/fl} Cx3cr1-cre* primary macrophages after stimulated with T-DNA for 8 hours.

(D) LDH release analysis of *Cx3cr1-cre*, *Gsdmd^{fl/fl} Cx3cr1-cre* and *Aim2^{fl/fl} Cx3cr1-cre* primary macrophages after stimulated with T-DNA for 8 hours.

Data are representative of two independent experiments for (A) and data are pooled from two independent experiments for (B), data are representative of three independent experiments for (C) and data are pooled from three independent experiments for (D). Error bars show mean \pm sem. * $P \leq 0.05$, ** $P \leq 0.01$, *** $P \leq 0.001$, **** $P \leq 0.0001$. Two-tailed unpaired student's *t*-test for (B and D).



Supplementary Figure 7. GSDMD attenuates the activation of cGAS-STING signaling following T-DNA stimulation primarily dependent on pyroptosis but partially through K⁺ efflux. Related to Figure 3.

(A) Immunoblot analysis of cell extracts from WT and *Gsdmd*^{-/-} primary macrophages after stimulated with T-DNA in the presence of DMF (25μM) for 8 hours.

(B) LDH release analysis of WT and *Gsdmd*^{-/-} primary macrophages after stimulated with T-DNA in the presence of DMF (25μM) for 8 hours.

(C) qPCR analysis of *Sting1* of WT and *Gsdmd*^{-/-} primary macrophages after stimulated with T-DNA in the presence of DMF (25μM) for 8 hours.

(D) qPCR analysis of *Oas1l* of WT and *Gsdmd*^{-/-} primary macrophages after stimulated with T-DNA in the presence of DMF (25μM) for 8 hours.

(E) Representative flow cytometry plots of p-TBK1 of WT and *Gsdmd*^{-/-} primary macrophages after stimulated with T-DNA in the presence of DMF (25μM) for 8 hours.

(F) Analysis of p-TBK1 of WT and *Gsdmd*^{-/-} primary macrophages after stimulated with T-DNA in the presence of DMF (25μM) for 8 hours.

(G) Immunoblot analysis of cell extracts from WT and *Gsdmd*^{-/-} primary macrophages after stimulated with T-DNA in the presence of KCl (50mM) for 8 hours.

(H) LDH release analysis of WT and *Gsdmd*^{-/-} primary macrophages after stimulated with T-DNA in the presence of KCl (50mM) for 8 hours.

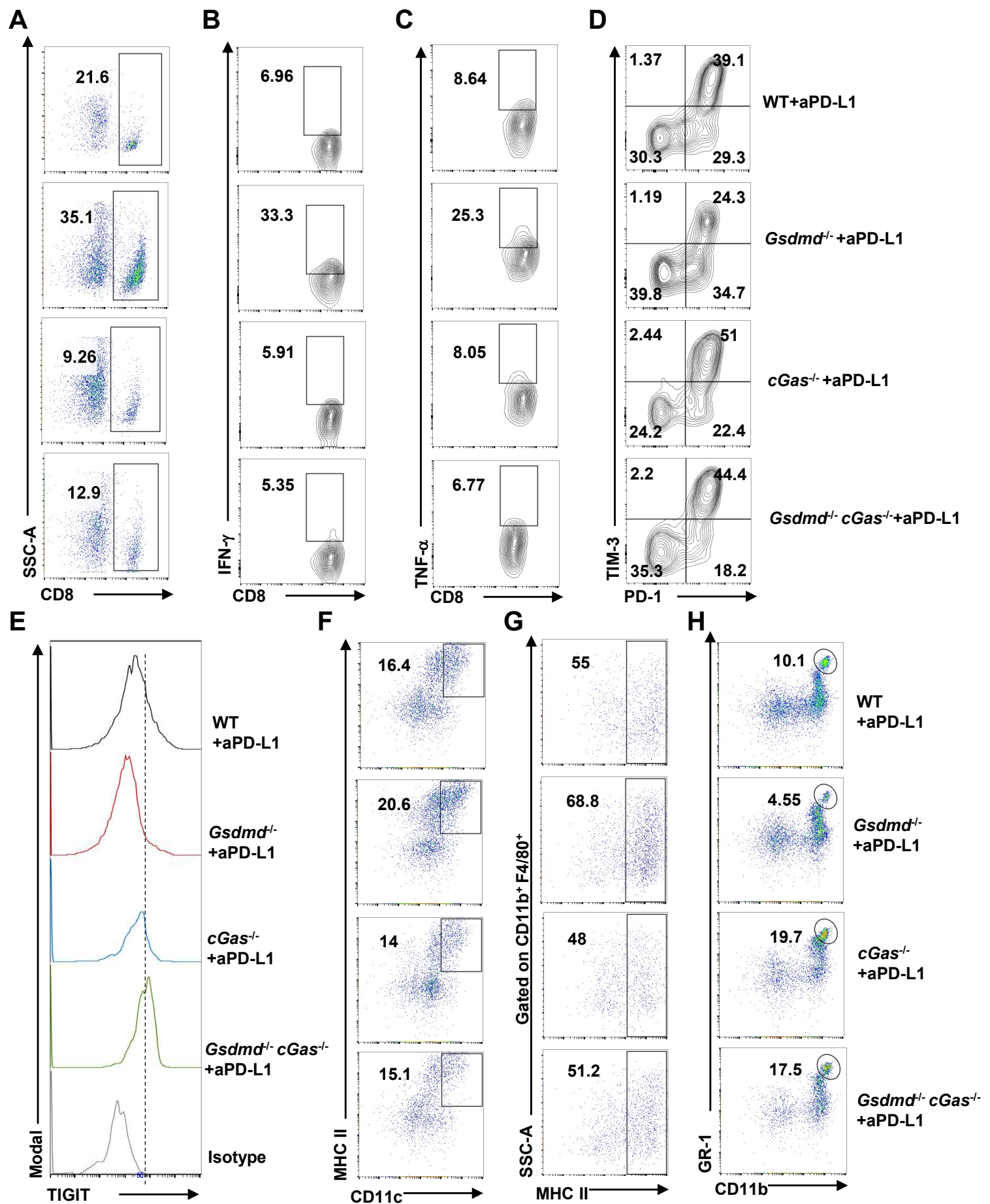
(I) qPCR analysis of *Sting1* of WT and *Gsdmd*^{-/-} primary macrophages after stimulated with T-DNA in the presence of KCl (50mM) for 8 hours.

(J) qPCR analysis of *Oas1l* of WT and *Gsdmd*^{-/-} primary macrophages after stimulated with T-DNA in the presence of KCl (50mM) for 8 hours.

(K) Representative flow cytometry plots of p-TBK1 of WT and *Gsdmd*^{-/-} primary macrophages after stimulated with T-DNA in the presence of KCl (50mM) for 8 hours.

(L) Analysis of p-TBK1 of WT and *Gsdmd*^{-/-} primary macrophages after stimulated with T-DNA in the presence of KCl (50mM) for 8 hours.

Data are representative of three independent experiments for (A, E, G and K) and data are pooled from three independent experiments for (B-D, F, H-J and L). Error bars show mean ± sem. **P* ≤ 0.05, ***P* ≤ 0.01, ****P* ≤ 0.001, *****P* ≤ 0.0001, ns, not significant. Two-tailed unpaired student's *t*-test for (B-D, F, H-J and L).



Supplementary Figure 8. GSDMD deficiency enhances cGAS-dependent antitumor immunity. Related to Figure 4.

(A) Representative flow cytometry plots of CD8⁺ T cells in Figure 4C.

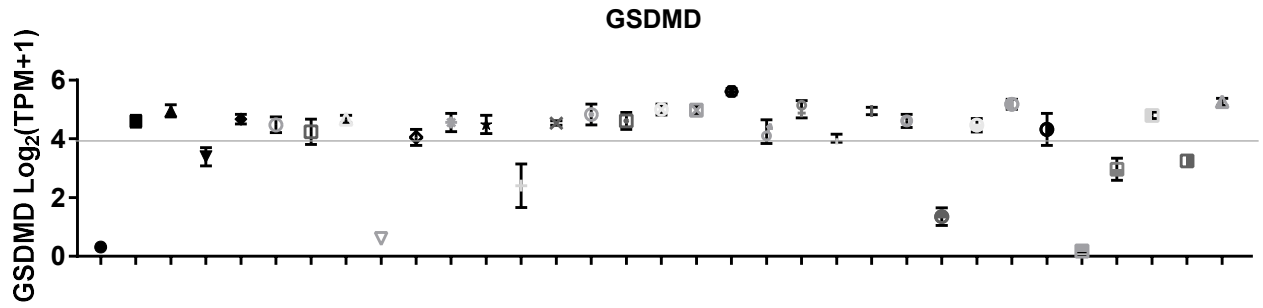
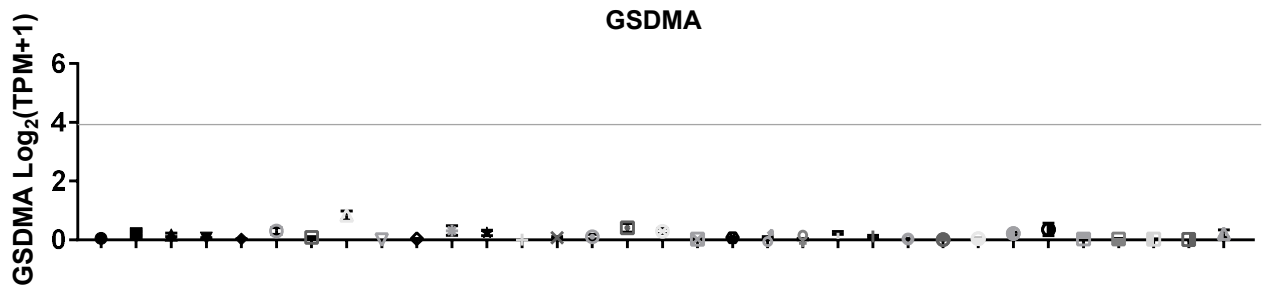
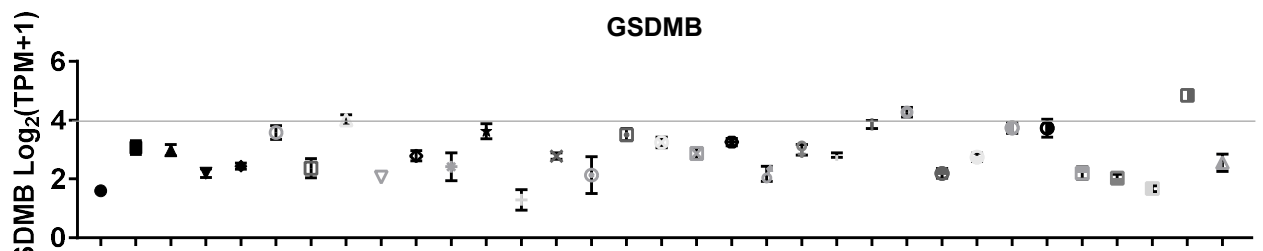
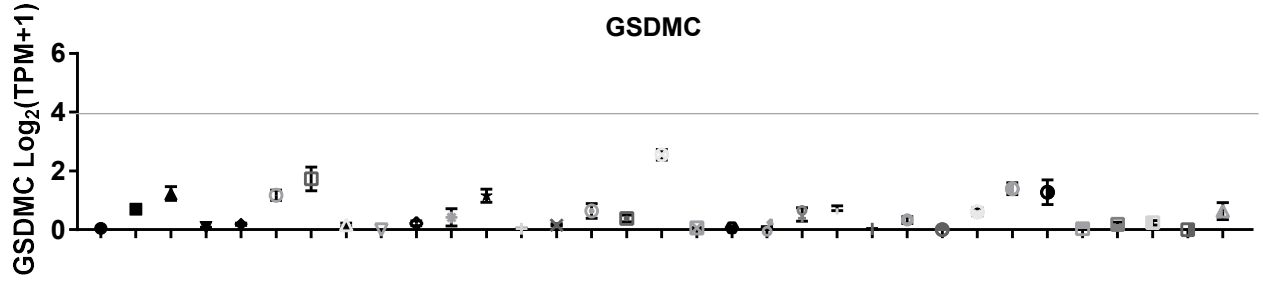
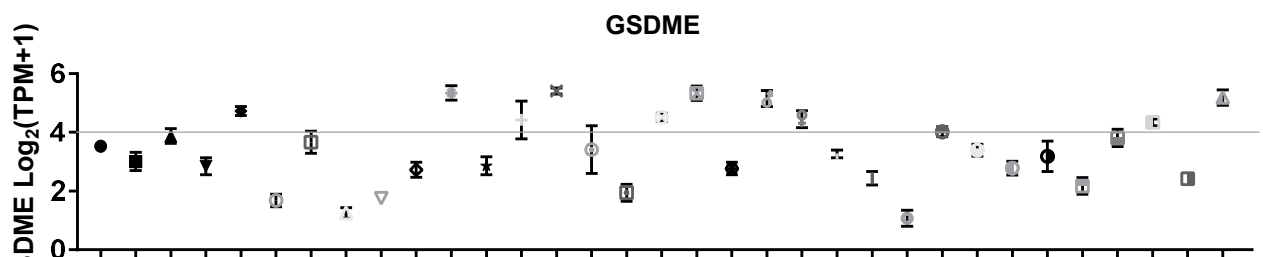
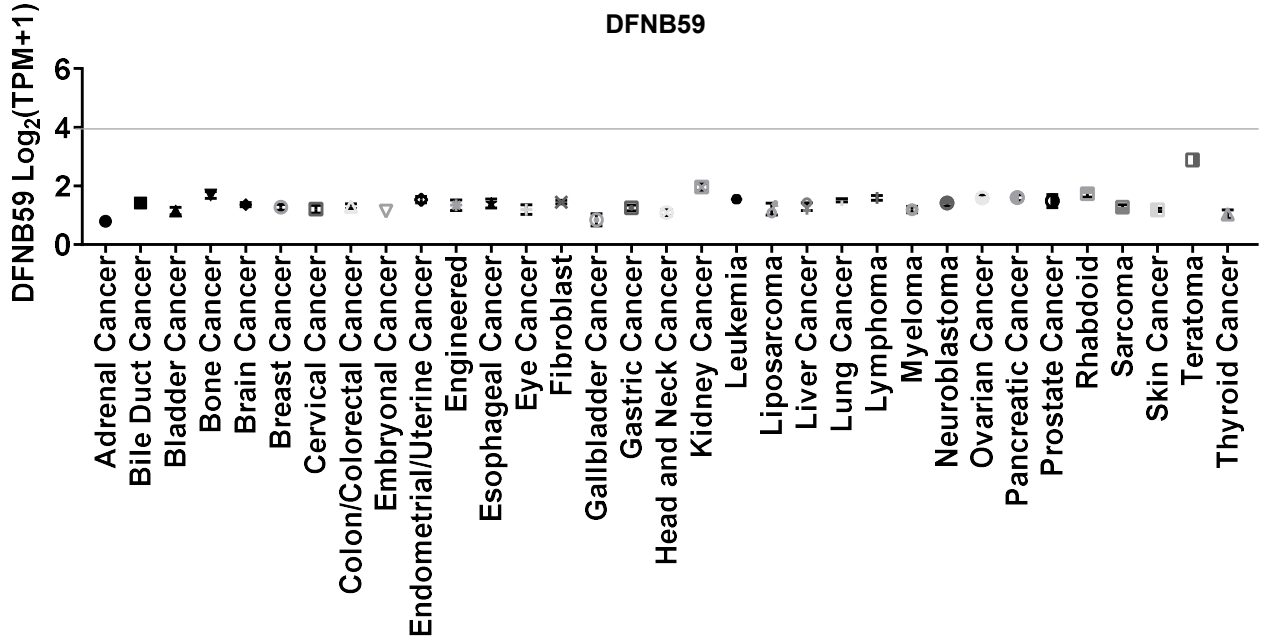
(B-C) Representative flow cytometry plots of CD8⁺ IFN-γ⁺ (B) and TNF-α⁺ (C) T cells in Figure 4D-G.

(D) Representative flow cytometry plots of PD-1 and TIM-3 expression in CD8⁺ T cells in Figure 4H-I.

(E) Representative flow cytometry plots of TIGIT expression in CD8⁺ T cells in Figure 4J.

(F-H) Representative flow cytometry plots of DCs (F), MHC II⁺ macrophages (G) and MDSCs (H) in Figure 4K-M.

Data are representative of three independent experiments for (A-H).

A**B****C****D****E****F**

Supplementary Figure 9. GSDMD is highly expressed in 33 different types of tumor cells. Related to Figure 4.

(A) CCLE data showed the expression of GSDMD in different types of tumor cells.

(B) CCLE data showing the expression of GSDMA in different types of tumor cells.

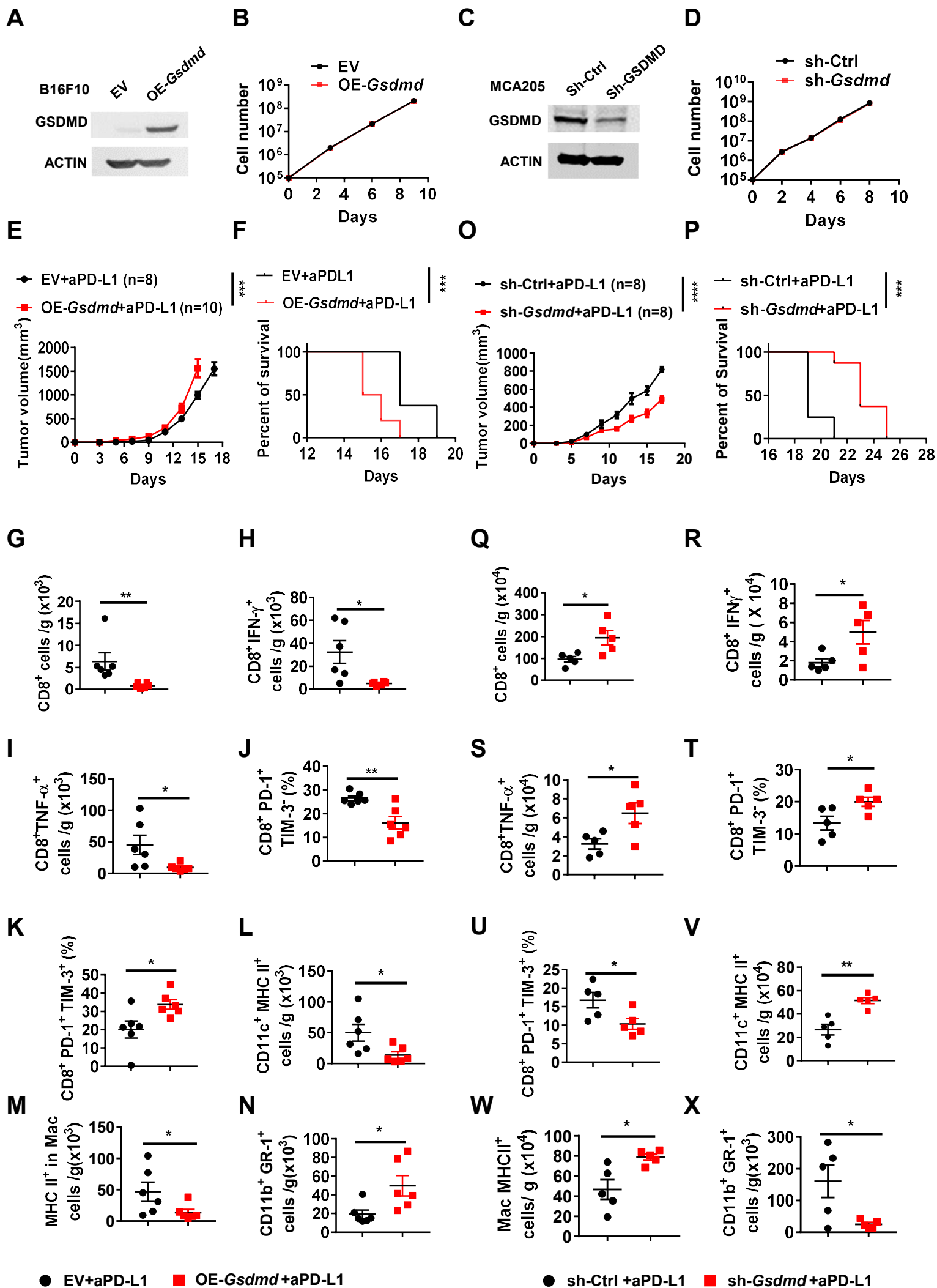
(C) CCLE data showing the expression of GSDMB in different types of tumor cells.

(D) CCLE data showing the expression of GSDMC in different types of tumor cells.

(E) CCLE data showing the expression of GSDME in different types of tumor cells.

(F) CCLE data showing the expression of GFNB59 in different types of tumor cells.

(A-F), Expression of indicated genes are shown by $\text{Log}_2(\text{TPM}+1)$.



Supplementary Figure 10. GSDMD in tumor cells restrains antitumor immunity. Related to Figure 4.

(A, C) Immunoblot analysis of GSDMD expression in EV (empty vector) or OE-*Gsdmd* (overexpress- *Gsdmd*) B16F10 cells (A), and sh-Ctrl or sh-*Gsdmd* MCA205 cells (C).

(B, D) Numbers of EV or OE-*Gsdmd* B16F10 cells (B) and sh-Ctrl or sh-*Gsdmd* MCA205 cells (D) in cell culture were monitored at indicated times (n = 3 per group).

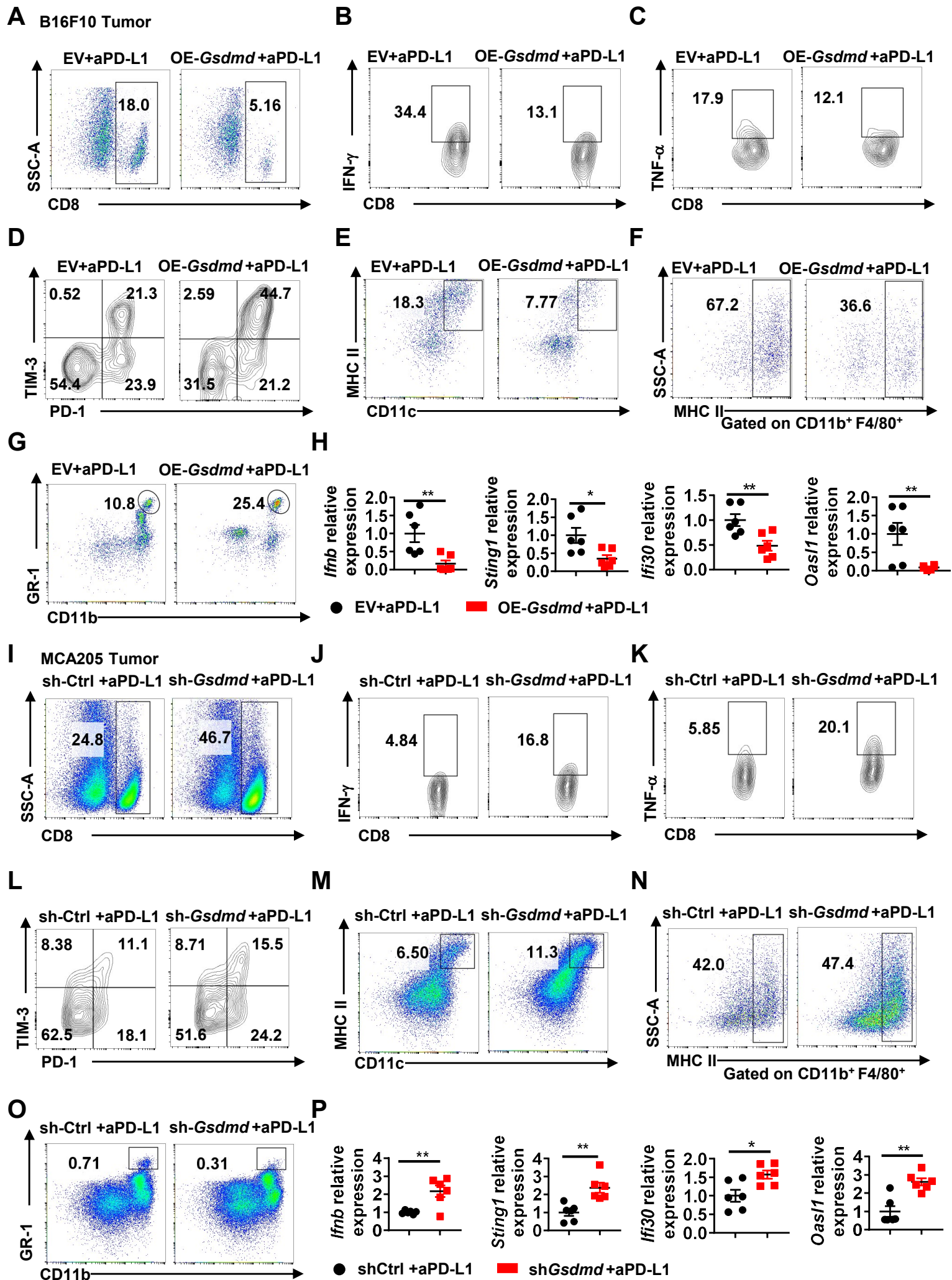
(E-F) WT mice were implanted subcutaneously with the same number of EV or OE-*Gsdmd* B16F10 cells and intraperitoneally injected with aPD-L1 on day 4 and 8. The growth of B16F10 cells (E) and the survival of mice (F) were assessed.

(G-N) 14 days later after implantation, tumors were collected for flow cytometry analysis of indicated cells (n = 6 mice per group).

(O-P) WT mice were implanted subcutaneously with same number of sh-Ctrl or sh-*Gsdmd* MCA205 cells and intraperitoneally injected with aPD-L1 on day 4 and 8. The growth of MCA205 cells (O) and the survival of mice (P) were assessed.

(Q-X) 14 days later after implantation, tumors were collected for flow cytometry analysis of indicated cells (n = 6 mice per group).

Data are pooled from two independent experiments for (E-F, O-P) and three independent experiments for (G-N, Q-X). Error bars show mean \pm sem. * $P \leq 0.05$, ** $P \leq 0.01$, *** $P \leq 0.001$, **** $P \leq 0.0001$. Two-way ANOVA test for tumor size, log-rank test for survival in (E-F, O-P). Two-tailed unpaired student's *t*-test for (G-N, Q-X).



Supplementary Figure 11. GSDMD deficiency in tumor cells improved antitumor immunity through ISGs. Related to Figure 4.

(A) Representative flow cytometry plots of CD8⁺ T cells in Figure S10G.

(B-C) Representative flow cytometry plots of CD8⁺ IFN- γ ⁺ (B) and TNF- α ⁺ (C) T cells in Figure S10H-I.

(D) Representative flow cytometry plots of PD-1 and TIM-3 expression in CD8⁺ T cells in Figure S10J-K.

(E-G) Representative flow cytometry plots of DCs (E), MHC II⁺ macrophages (F) and MDSCs (G) in Figure S10L-N.

(H) WT mice were implanted subcutaneously with same number of EV or OE-GSDMD B16F10 cells and intraperitoneally injected with aPD-L1 on day 4 and 8. Tumors were collected on day 14 for qPCR analysis of *IFN- β* , *Sting1*, *IFI30* and *Oas1l*.

(I) Representative flow cytometry plots of CD8⁺ T cells in Figure S10Q.

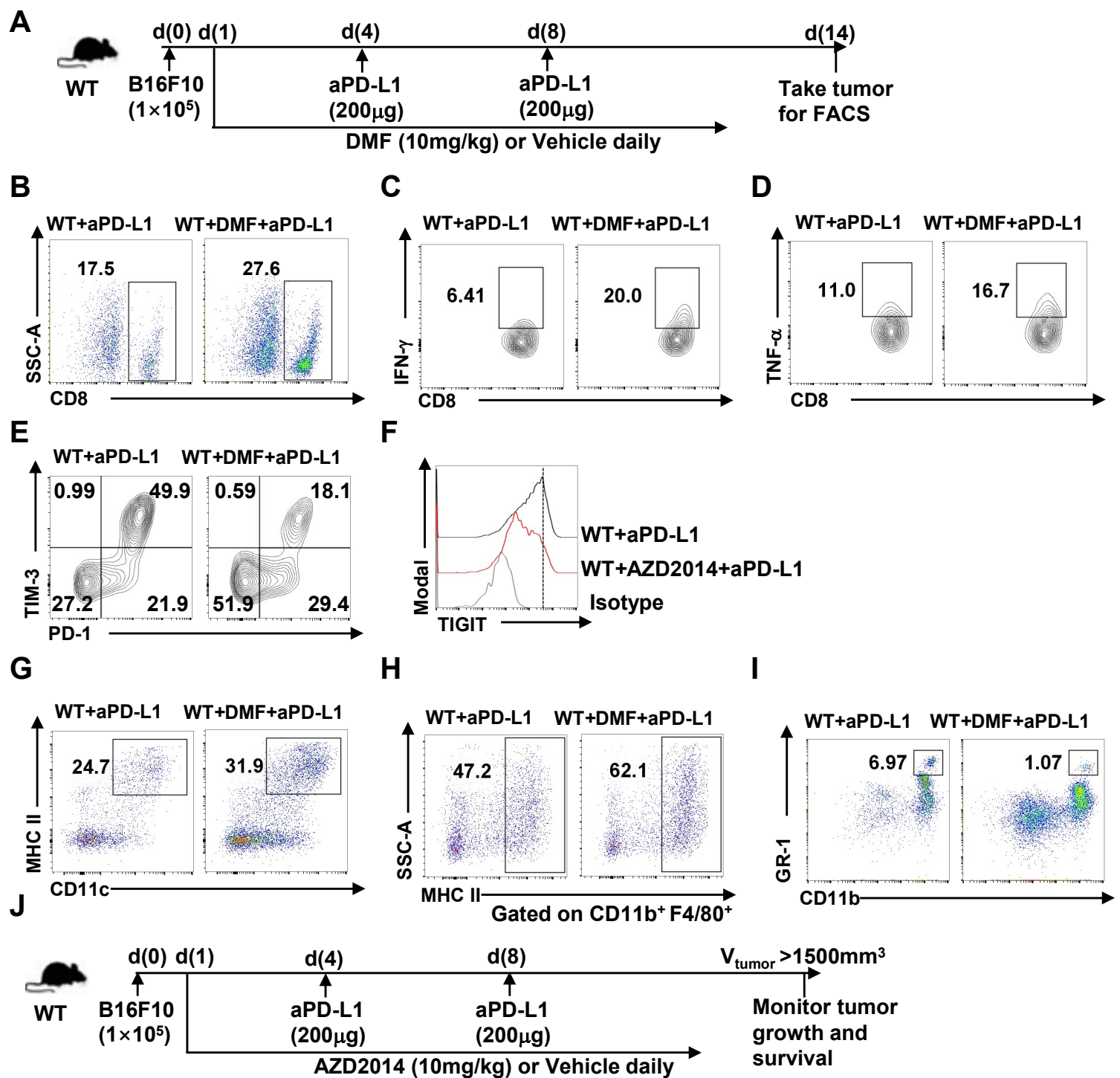
(J-K) Representative flow cytometry plots of CD8⁺ IFN- γ ⁺ (J) and TNF- α ⁺ (K) T cells in Figure S10R-S.

(L) Representative flow cytometry plots of PD-1 and TIM-3 expression in CD8⁺ T cells in Figure S10T-U.

(M-O) Representative flow cytometry plots of DCs (M), MHC II⁺ macrophages (N) and MDSCs (O) in Figure S10V-X.

(P) WT mice were implanted subcutaneously with same number of sh-Ctrl or sh-GSDMD MCA205 cells and intraperitoneally injected with aPD-L1 on day 4 and 8. Tumors were collected on day 14 for qPCR analysis of *Ifnb*, *Sting1*, *Ifi30* and *Oas1l*.

Data are pooled from three independent experiments for (H, P), and data are representative of three independent experiments for (A-G, I-O). Error bars show mean \pm sem. * $P \leq 0.05$, ** $P \leq 0.01$. Two-tailed unpaired student's *t*-test for (H, P).



Supplementary Figure 12. Pharmacological inhibition of GSDMD promotes antitumor immunity in combination with PD-L1 antibody treatment. Related to Figure 5.

(A) Schematic representation of the experiments in Figure 5C-L. 1×10^5 B16F10 cells were implanted subcutaneously into WT mice, and aPD-L1 (200 μ g) were intraperitoneally injected on day 4, 8 with or without DMF (10mg/kg) intraperitoneally injected every day after implantation. Tumors were collected on day 14.

(B) Representative flow cytometry plots of CD8⁺ T cells in Figure 5C.

(C-D) Representative flow cytometry plots of CD8⁺ IFN- γ ⁺ (C) and TNF- α ⁺ (D) T cells in Figure 5D-G.

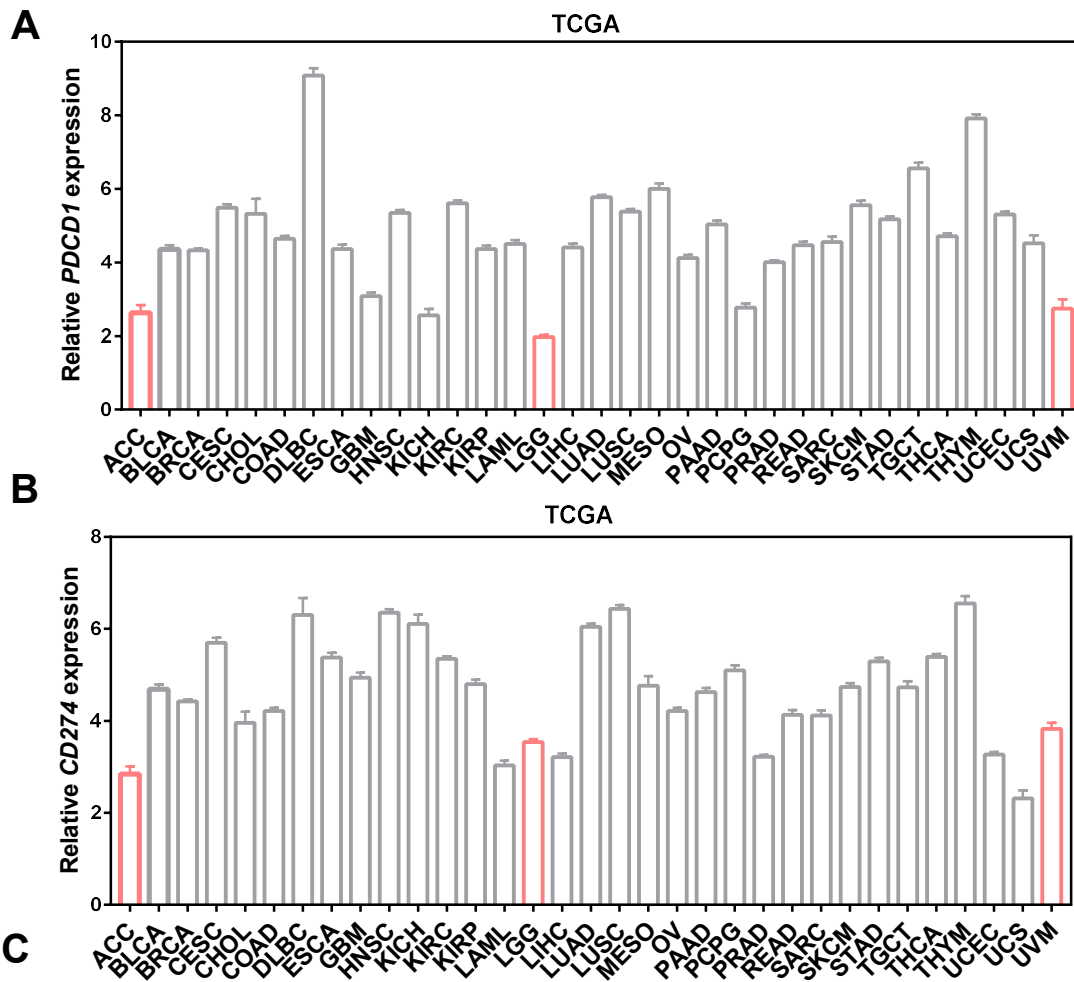
(E) Representative flow cytometry plots of PD-1 and TIM-3 expression in CD8⁺ T cells in Figure 5H.

(F) Representative flow cytometry plots of TIGIT expression in CD8⁺ T cells in Figure 5I.

(G-I) Representative flow cytometry plots of DCs (G), MHC II⁺ macrophages (H) and MDSCs (I) in Figure 5J-L.

(J) Schematic representation of the experiments in Figure 5M-N. 1×10^5 B16F10 cells were implanted subcutaneously into WT and *Gsdmd*^{-/-} mice, and aPD-L1 (200 μ g) were intraperitoneally injected on day 4, 8 with or without AZD2014 (10mg/kg) intraperitoneally injected daily after implantation. Tumor volumes and mice survival were assessed every other day from day 7. Mice were euthanized when tumor volumes exceeded 1500mm³.

Data are representative of three independent experiments for (B-I).



Supplementary Figure 13. Model for GSDMD function in antitumor immunity. Related to Figure 5.

(A) Gene expression of *PDCD1* in different kinds of tumors was analyzed using the data from TCGA database.

(B) Gene expression of *CD274* in different kinds of tumors was analyzed using the data from TCGA database.

(C) GSDMD deficiency facilitates CD8⁺ T cell antitumor immunity by promoting ISG program in APCs in response to anti-PD-L1 treatment.

Error bars show mean \pm sem.